40364

National Library of Canada | Bibliothèque nationale du Canada

CANADIAN THESES ON MICROFICHE | THÈSES CANADIENNES SUR MICROFICHE

NAME OF AUTHOR/NOM DE L'AUTEUR Jaeshin Ahn

TITLE OF THESIS/TITRE DE LA THÈSE Ion Beam Deposition of Multilayer Metallic Thin Films

UNIVERSITY/UNIVERSITÉ University of Alberta

DEGREE FOR WHICH THESIS WAS PRESENTED/GRADE POUR LEQUEL CETTE THÈSE FUT PRÉSENTÉE M.Sc.

YEAR THIS DEGREE CONFERRED/ANNÉE D'OBTENTION DE CE GRADE 1979

NAME OF SUPERVISOR/NOM DU DIRECTEUR DE THÈSE Dr. R.P.W. Lawson

Permission is hereby granted to the NATIONAL LIBRARY OF CANADA to microfilm this thesis and to lend or sell copies of the film.

The author reserves other publication rights, and neither the thesis nor extensive extracts from it may be printed or otherwise reproduced without the author's written permission.

L'autorisation est, par la présente, accordée à la BIBLIOTHÈQUE NATIONALE DU CANADA de microfilmer cette thèse et de prêter ou de vendre des exemplaires du film.

L'auteur se réserve les autres droits de publication; ni la thèse ni de longs extraits de celle-ci ne doivent être imprimés ou autrement reproduits sans l'autorisation écrite de l'auteur.

DATED/DATÉ Apr 5, 1979 SIGNED/SIGNÉ J Ahn

PERMANENT ADDRESS/RÉSIDENCE FIXE 433 Michener Park Edmonton, Alberta

NL-91 (3-74)

National Library of Canada

Cataloguing Branch
Canadian Theses Division

Ottawa, Canada
K1A 0N4

Bibliothèque nationale du Canada

Direction du catalogage
Division des thèses canadiennes

NOTICE

The quality of this microfiche is heavily dependent upon the quality of the original thesis submitted for microfilming. Every effort has been made to ensure the highest quality of reproduction possible.

If pages are missing, contact the university which granted the degree.

Some pages may have indistinct print especially if the original pages were typed with a poor typewriter ribbon or if the university sent us a poor photocopy.

Previously copyrighted materials (journal articles, published tests, etc.) are not filmed.

Reproduction in full or in part of this film is governed by the Canadian Copyright Act, R.S.C. 1970, c. C-30. Please read the authorization forms which accompany this thesis.

THIS DISSERTATION
HAS BEEN MICROFILMED
EXACTLY AS RECEIVED

AVIS

La qualité de cette microfiche dépend grandement de la qualité de la thèse soumise au microfilmage. Nous avons tout fait pour assurer une qualité supérieure de reproduction.

S'il manque des pages, veuillez communiquer avec l'université qui a conféré le grade.

La qualité d'impression de certaines pages peut laisser à désirer, surtout si les pages originales ont été dactylographiées à l'aide d'un ruban usé ou si l'université nous a fait parvenir une photocopie de mauvaise qualité.

Les documents qui font déjà l'objet d'un droit d'auteur (articles de revue, examens publiés, etc.) ne sont pas microfilmés.

La reproduction, même partielle, de ce microfilm est soumise à la Loi canadienne sur le droit d'auteur, SRC 1970, c. C-30. Veuillez prendre connaissance des formules d'autorisation qui accompagnent cette thèse.

LA THÈSE A ÉTÉ
MICROFILMÉE TELLE QUE
NOUS L'AVONS REÇUE

THE UNIVERSITY OF ALBERTA

Ion Beam Deposition of Multilayer Metallic Thin Films

by

Jaeshin Ahn

(C)

A THESIS

SUBMITTED TO THE FACULTY OF GRADUATE STUDIES AND RESEARCH

IN PARTIAL FULFILMENT OF THE REQUIREMENTS FOR THE DEGREE

OF Master of Science

Department of Electrical Engineering

EDMONTON, ALBERTA

SPRING, 1979

THE UNIVERSITY OF ALBERTA

FACULTY OF GRADUATE STUDIES AND RESEARCH

The undersigned certify that they have read, and recommend to the Faculty of Graduate Studies and Research, for acceptance, a thesis entitled Ion Beam Deposition of Multilayer Metallic Thin Films

submitted by Jaeshin Ahn

in partial fulfilment of the requirements for the degree of Master of Science

in Electrical Engineering.

Randall W Lane
.....

Supervisor

Douglas M. Sheppard
.....

F.E. Vermeulen
.....

Date January 22, 1979
.....

ABSTRACT

An innovative thin film deposition technique : low energy ion beam deposition , is further studied. The theoretical deposition processes of this method are discussed. Double layer thin films of Mg and Pb on carbon substrates are produced by this method and compared with similar films grown by thermal evaporation. Their characteristics are investigated by Rutherford backscattering analysis and Scanning Electron Microscopy. The RBS technique is expanded to derive a profile of composition ratio versus depth within the deposits and applied to a depth analysis of the double layer films. The present study of film characteristics shows that a high level of mass selectivity is observed from the low energy ion beam deposited Mg films. The oxidation of Mg films is not limited to the film surface : oxygen is seen to be distributed into the Mg region rather than staying on the surface. The preferential migration of Pb into Mg is observed and the diffusion coefficient of Pb into Mg at 300° C is calculated as 1.236×10^{-19} cm²/sec. The interdiffusion region between the Mg and Pb film layer ranges from 1000 to 3000 Å at room temperature.

Acknowledgement

The author wishes to thank his supervisor, Dr. R.P.W. Lawson for his help and encouragement during the course of this work and throughout the writing of this thesis.
The author owes a debt of gratitude to his lovely wife, Taehui, for her encouragement and understanding during this work.
The author would also like to express his appreciation to the following people.

Dr. G.C. Neilson, Dr. H. Fielding, Dr. Nam and researchers at the Nuclear Research Center, for use of the Van de Graaff Accelerator.

Dr. B. Schneider, for use of the SEM.

Dr. J. Amano, for helpful guidance over the deposition system.

Mr. R. Schmaus, for maintenance of the system.

The National Research Council of Canada and the University of Alberta, for their financial support.

Table of Contents

Chapter	Contents	Page
1	INTRODUCTION	1
2	THE LOW ENERGY ION BEAM DEPOSITION PROCESS	7
2.1	Introduction	7
2.2	Neutralization of ions on the metal surface and emission of secondary electrons	8
2.3	Collison between the incident particle and a target atom	12
2.4	Nucleation and growth	14
2.5	Diffusion of thin films	17
2.6	Thermal diffusion	18
3	THE LOW ENERGY ION BEAM DEPOSITION SYSTEM	22
3.1	Vacuum system	22
3.2	Ion beam system	23
4	RUTHERFORD BACKSCATTERING FOR THIN FILM ANALYSIS	36
4.1	Mass resolution	36
4.2	Depth resolution	37
4.3	Density resolution	39
4.4	Composition resolution	43
4.5	Composition analysis of multilayer thin film	45
4.6	Composition analysis applied to the Pb-Mg-O-C combination	47

5 EXPERIMENTAL RESULTS AND DISCUSSION..... 57

5.1 Production of thin films..... 57

5.2 Van de Graaff accelerator preparation for Rutherford backscattering analysis..... 59

5.3 Stopping power and energy straggling data..... 63

5.4 Analysis of Rutherford backscattering spectra.... 65

6 CONCLUSIONS..... 107

REFERENCES..... 109

LIST OF TABLES

TABLE	DESCRIPTIONS	PAGE
1-1 :	Comparison of the low energy ion beam deposition method with conventional techniques.	5
2-1 :	Work function and ionization energy	13
4-1 :	Atomic density for standards bulk material	56
5-1 :	Stopping power data ($_4He^+$)	66
5-2 :	The isotopes of Mg	74
5-3 :	Oxidation rate of Mg	77

LIST OF FIGURES

FIGURE	DESCRIPTIONS	PAGE
3-1	Schematic diagram of differential pumping system	24
3-2	Schematic diagram of vacuum system	25
3-3	Schematic diagram of ion source	27
3-4	Low energy ion beam deposition system	28
3-5	Geometry and mass separation in E x B separator.	29
3-6	Cross section of velocity filter	31
3-7	Substrate chamber	33
3-8	Block diagram of system electronics	35
4-1	Particles energy in the process of backscattering.	40
4-2	Backscattering yield from a slab of target material	42
4-3	Backscattered particle energy from different scattering centers in compound target	52
4-4	Stopping power data ($_4He^+$)	54
5-1	RBS data handling system	61
5-2	Secondary electron emission from RBS target	62
5-3	RBS detector geometry	64
5-4	Energy straggling in backscattering experiment of 2.0 MeV $_4He^+$ with Pb and Mg target	67
5-5	Background level removal	71
5-6	RBS spectra of CM(T) and CM(48)	73

5-7 Depth profile of CM(T)..... 78
5-8 Depth profile of CM(48)..... 79
5-9 RBS spectra of CM(48)P(48)..... 82
5-10 RBS spectra of CP(48)M(48)..... 83
5-11 Depth profile of CM(48)P(48)..... 84
5-12 Depth profile of CP(48)M(48)..... 85
5-13 SEM surface topography of CM(48) and CP(48)..... 87
5-14 SEM surface topography of carbon substrate..... 89
5-15 SEM surface topography of CM(T) and CM(48)..... 92
5-16 SEM surface topography of CM(T)P(T) and CM(48)P(48)..... 94
5-17 RBS spectra of CP(T)M(48) ; as deposited, after 300° C - 30 min. and after 320° C - 250 min. annealing..... 98
5-18 Mg and oxygen portion of figure 5-17 in expanded energy scale..... 99
5-19 Pb portion of figure 5-17 in expanded energy scale..... 100
5-20 Depth profile of CP(T)M(48) ; as deposited..... 101
5-21 Depth profile of CP(T)M(48) ; after 30 min. annealing at 100° C..... 102
5-22 Depth profile of CP(T)M(48) ; after 30 min. annealing at 200° C..... 103
5-23 Depth profile of CP(T)M(48) ; after 30 min. annealing at 300° C..... 104
5-24 Depth profile of CP(T)M(48) ; after 250 min. annealing at 320° C..... 105

5-25 Pb atomic concentration slope in Mg region before and after 300° C - 30 min. annealing..... 106

CHAPTER 1

INTRODUCTION

The technology and understanding of thin films has advanced tremendously in recent years because of an industrial demand for microelectronic devices and optical coatings. In 1852 Bunsen and Grove (*1) obtained the first thin films by chemical reaction and glow-discharge sputtering techniques. Faraday (*1) also produced metal films by thermal evaporation in 1857. Since these initial efforts the techniques of thermal evaporation and glow discharge sputtering have been most frequently used for thin film production. With the advent of high power laser technology the need for high damage threshold material is apparent.

The damage to the optical interface is considered the limit of laser performance and the properties of the optical interface is limited by the film inhomogeneities, non linear susceptibility or weak absorption (*2). Various kinds of films have been made for laser optics. Most of these films are made by deposition of film material by evaporation or by sputtering onto a suitable substrate material. In both methods the substrate is within a high pressure environment as is the source of the coating material, a procedure which

increases the risk of contamination . The production of thin films by using a low energy, mass analyzed metallic ion beam under ultra high vacuum conditions was successfully demonstrated by Amano et. el.(*3). The characteristics of single layer films of lead and magnesium deposited on the carbon substrate by a low energy ion beam technique was investigated by Amano et. al.(*4).

In the low energy ion beam deposition method, the coating material itself is converted into an ion beam which is mass and energy analyzed and then transported to a differentially pumped chamber in which the substrate resides under ultra high vacuum conditions. Film growth proceeds when the ion beam is retarded to an energy low enough to minimize substrate or film damage but high enough to produce a good bond to the substrate.

The controllability of the ionized beam contributes favorably to the deposited film characteristics. A detailed comparison is outlined in Table 1-1.

The purpose of this thesis is to investigate characteristics of low energy ion beam deposited double layer films of lead and magnesium and to compare them with those made by a thermal evaporation method.

A Rutherford backscattering analysis method is chiefly employed to analyze the films. Film surface structure is determined by a scanning electron microscope and the chemical composition of magnesium films is confirmed by ESCA(Electron Spectroscopy for Chemical Analysis).

A computer program is written to translate the RBS(Rutherford BackScattering) spectra into physical depth and atomic concentration profiles.

The following example explains the convention used in this thesis to identify the film material in order of deposition and the method of deposition.

A number in parentheses following a letter identifies that material having been deposited by the IBD technique at the energy (in eV) denoted by the number. The letter T in parentheses following a letter identifies a thermally evaporated film. The order of the letters after C (the carbon substrate) identifies the order of deposition.

ex) CM(48)P(T)

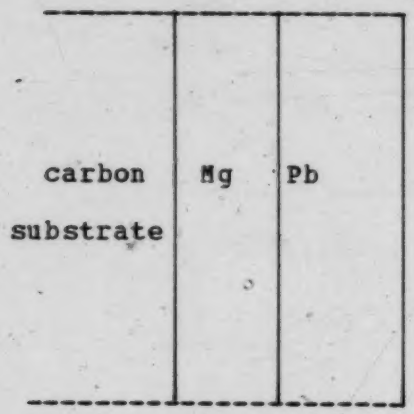

CM(48)P(T) identifies a carbon substrate with a magnesium

film ion beam deposited at 48 eV energy, follwed by a thermally evaporated lead layer.

Table 1-1
Comparison of the low energy ion beam deposition method to conventional techniques

	low energy ion beam deposition	thermal evaporation	sputtering
incident particle	ion	molecule	atom, molecule, ion
pressure during film growth	$< 1 \times 10^{-5}$ torr	$\sim 10^{-6}$ torr	$10^{-5} \sim 10^{-6}$ torr
incident particle energy	$\sim$ 50 eV (*2) Variable	0.18 eV (*1)	0 $\sim$ 50 eV
particle status	ionized	neutral, excited, ionized, or a combi-nation of these	
film growth rate	controlled by ion beam current and energy	governed by source T, pressure and distance between substrate and source	governed by ion energy, species, incident angle and target species
directionallity	well focused onto the substrate	from the point source particle moves away in all directions with equal probabiliy.	uncontrollable, varies depending on ion species, energy and target material

(*1) average kinetic energy of particle with T=1200°K
(*2) the optimum energy for Mg and Pb ion.

	low energy ion beam deposition	thermal evaporation	sputtering
thickness control	controlled by the total deposited	should be monitored by proper thickness monitor during deposition	
film material selectivity	mass is analyzed by E x B filter	rely on the source material purity and the pressure during the deposition	rely on the target material purity and the pressure during the deposition
film thickness distribution	ion beam can be scanned over desired area with programmed speed, producing uniform thickness	depends on the source type, distance between the source and substrate, pressure during deposition	depends on ion energy, species, target material. needs mechanical movement of sustrate during sputtering to improve thickness distribution
generation of pattern	beam can be scanned with programmed speed and current producing desired pattern	deposition masking or subtractive etching after deposition	
film material	limited by ionizability of the material	unlimited	
productivity	due to small ion beam current, productivity is low	good for mass production	

CHAPTER 2

THE LOW ENERGY ION BEAM DEPOSITION PROCESS

2.1 Introduction

Starting from the energetic ions moving towards a target until the film forms on the conductive target, the following processes are considered to be happening. The following is just a summary of the processes and they will be discussed in more detail in later sections.

a ; The ions are neutralized near the conductive target surface before the kinetic collison process can occur.

b ; As the neutralized atom moves closer to the target surface, the kinetic energy of the neutralized atom is transferred to the target by elastic collisions because the initial energy of the incident ion is low (*1).

c ; Losing kinetic energy, the adatom will be accommodated to the surface causing nuclei to form; the nuclei grow in three dimensions forming islands and the islands grow until they touch. The neighboring islands coalesce, forming larger islands. As the islands continue to grow, the

tendency of maintaining roundness after coalescence decreases. The islands become elongated and join to form continuous networks leaving long and narrow channels between them. As the deposition proceeds, the channels are filled and a continuous film is formed.

d ; During and after the deposition process, diffusion of the film material occurs in three dimensions.

e ; When the kinetic energy of the ion is higher than the threshold energy for displacement of the film material, self-sputtering adversely affects the film growth.

2.2 Neutralization of ions on the metal surface and emission of secondary electrons.

In considering the interaction between an ion and a metal atom when an ion is approaching the metal surface, it is convenient to distinguish between the kinetic energy and potential energy of the ion. The kinetic energy is provided by the acceleration potential, usually applied between the ion source and target, while the potential energy is given by the ionization process.

For low energy incoming ions interacting with target material, the transfer of kinetic energy from the former to atoms of the latter can be adequately described using hard

sphere collision models(*2). For high energy incident ions the kinetic energy transfer is inelastic which involves the energy transfer not only in nuclear motion but also in excitation and ionization of the electrons of the target atom.

The secondary electron emission yield is independent of ion energy when the ion energy is less than 1 KeV and potential ejection predominates in this region (*3). At energies greater than 1 KeV, kinetic ejection is not negligible and the yield increases, initially linearly with the kinetic energy of the ion and later linearly with velocity, eventually approaching a maximum, before decreasing (*4,*5). It was found by Hagstrum (*6) that for low energy ions, the neutralization process occurs with a high probability before the kinetic process can occur. The following neutralization processes of ions near the metal surface were studied by various researchers (*7,*8,*9,*10).

a Resonance neutralization

b Resonance ionization

c Auger de-excitation

d Auger neutralization

The resonance neutralization was first suggested by Oliphant and Moon (*11) and the process is written as,

$$A^{+} + N\,Em^{-} \text{ --------- } A^{*} + (N-1)\,Em^{-} \text{ -----(2-1)}$$

where

A^{+} ; incident ion

N ; the number of metal electrons

A^* ; excited atom

The process (2-1) can occur whenever the condition $e\bar{\phi} < Em_i <$ Wa is satisfied.

where

$e\bar{\phi}$; average work function of the metal Em ; electrons in the metal

Em_i ; the energy of metal electron relative to the Fermi level Wi

Wa ; outer work function of metal

The excited atom A^* may reverse the resonance neutralization process causing resonance ionization. This process is written as,

$$A^* \text{ ----------} \rightarrow A^+ + Em^- \text{--------} (2\text{-}2)$$

Also the excited atom in equation (2-1) may undergo Auger de-excitation . The process is written as,

$$A^* + N\ Em^- \text{ -------} \rightarrow A + E^- + (N-1)\ Em^- \text{ ----} (2\text{-}3)$$

This process can occur whenever the condition $eI > e\bar{\phi}$ is fullfilled.

where

eI ; the ionization energy of the incident particle.

Whenever the condition $E^* > e\bar{\phi}$ is fullfilled, secondary electrons, E^-, are emitted. E^* is excitation energy. The maximum kinetic enegy of the secondary electron ejected in an Auger de-excitation process is given by,

$$(Ee)max = E^* - e\bar{\phi} \text{ ---------} (2\text{-}4)$$

The resonance neutralization is followed by the Auger

de-excitation process to completely neutralize the ion. In contrast to resonance neutralization, which is a two step process, Auger neutralization is a single step process of ion neutralization on the conductive surface. The Auger neutralization process is written as,

$$A^{+} + N\,Em^{-} \longrightarrow A + E^{-} + (N-2)\,Em^{-} \quad \text{---(2-5)}$$

Two electrons from the conduction band of the target material are involved. One electron is used to neutralize the incident ion directly to the ground state and the other electron is ejected by the released energy from the transition of the ion. The maximum kinetic energy of the secondary electron from the Auger neutralization is given by,

$$(Ee)max = eI - 2e\phi \quad \text{----------(2-6)}$$

It is lower than that of the Auger de-excitation process. It was found by Hagstrum (*12) that Auger neutralization is more probable than resonance neutralization at low incident ion energies. Hagstrum's (*13) experimental results show that the maximum energy of secondary electrons ejected from Mo substrates irradated by He^{+} stays below (Ee)max for Auger neutralization when the incident ion energy is below 40 eV and for greater than 100 eV, the energy distribution of secondary electron was over (Ee)max for Auger neutralization showing resonance neutralization had occured. As suggested by Hagstrum (*14), the condition $eI > 2e\phi$ must be fullfilled to make Auger neutralization possible. From the work function and ionization data of carbon, lead and

magnesium, it is clear that the neutralization process of a singly charged low energy Pb ion depends mostly on the two step process, i.e., resonance neutralization and Auger de-excitation when the target surface is carbon or lead. When the target surface is Mg, the dominating neutralization process is Auger neutralization until the surface is covered by lead at which point the process changes into a two step one. For singly charged low energy Mg ions, the dominating neutralization process is a two step process when the target surface is carbon or lead but when the target surface is covered with Mg, the process turns to Auger neutralization. Table 2-1 (*15,*16) shows work function and ionization energy of carbon, magnesium and lead.

2.3 Collison between the incident particle and a target atom.

The ion beam energies employed for the experiment are less than 150 eV and the collison between a neutralized incident atom and a target atom is considered elastic. The hard sphere binary collison model can explain the kinetic energy transfer process. The total energy transferred to the target atom from the incident particle is given by (*17) ,

$$T=4M1M2/(M1 + M2)^2 Eo \sin^2\theta/2 \text{----------} (2-7)$$

where

T ; The transferred energy

Eo ; Incident particle kinetic energy

Table 2-1

Work function and ionization energy

	carbon	Mg	Pb
work function (eV)	4.39	3.46	4.02
ionization energy (eV) single		7.64	7.41
double		22.67	22.44

M1, M2 ; Incident particle and target atom weight

θ ; The deflection angle of incident particle after the collison in the center of mass system.

When θ=180°, i.e., the motion of incident particle is reversed or stopped after collison, the maximum energy transfer is given by,

$$T = 4\ M1\ M2\ Eo\ /(\ M1 + M2\ )^2 \qquad \text{----------(2-8)}$$

In an elastic collison between the incident particle and a target atom, hard spheres of radius R are used to explain the process. R is determined by the interatomic potential and the energy of the incident particle. Several theories (*18,*19,*20) discuss the interatomic potential but none is definitely valid for all interaction distances. It is suggested that for small approach distances, a Bohr potential may be reasonably employed while larger separation distances require a Born-Mayer model. For example, an incident copper ion having a kinetic energy of 50 eV and colliding with a copper atom will have the following hard sphere diameters depending on the choice of theory. They are given by,

0.722 Å: Bohr model

1.264 Å: Born-Mayer model

1.986 Å: Thomas-Fermi model

2.4 Nucleation and growth

The process of nucleation and growth of thin films was investigated theoretically by various researchers (*21,*22,*23) and the thermal-accomodation coefficient is defined as,

$$\alpha_T = (Ev - Er)/(Ev - E) = (Tv - Tr)/(Tv - T) \quad \text{------(2-9)}$$

where

Ev ; incident kinetic energy of the incident atom

Er ; energy of the desorbed atom before equilibration with the substrate

E ; energy of the desorbed atom after it has equilibrated with the substrate

Tv,Tr,T ; corresponding temperature

It is suggested (*24) that complete thermal accomodation, ie. $\alpha_T = 1$, is obtained when the incident atom kinetic energy is less than the activaton energy for desorption (approx. 0.5 eV). For thermally evaporated Mg and Pb atoms with kinetic energies of less than 0.17 eV per atom (equivalent to 2000° K), the thermal accomodation coefficient is unity and all the impinging atoms are equilibrated with the substrate without any rebounced atoms. For ion beams with incident kinetic energy of 50 eV, it is very likely that the thermal accomodation coefficient is less than unity because the incident kinetic energy is about 100 times the energy necessary for desorption after equilibration with the substrate and this ratio is beyond the suggested maximum value of 25 (*25) . During the initial stages of film

deposition by an ion beam with a kinetic energy of 50 eV, a fraction of the incident atoms bounce off the substrate causing a lower initial adsorption rate. The adsorbed atoms can either stick permanently to the substrate or reevaporate in a finite time. The following stages of film growth will be discussed for the adsorbed atoms ;

a The island stage

The adsorbed atoms migrate over the surface of the substrate and they constantly aggregate and dissociate until the cluster grows to a critical size. Beyond the critical sized nuclei, the cluster does not dissociate but becomes stable and grows to a larger permanent island.

b The coalescence stage

The islands continue to grow, and touch neighboring islands, coalescing to form a new island occupying an area smaller than the sum of the original two , thus exposing fresh substrate surface. New incident atoms are adsorbed on these freshly exposed areas and secondary nucleation occurs.

c The channel stage

As the islands continue to grow and coalesce and before a continuous film is made, a stage is reached in which the film consists of islands a few microns in lateral extent separated by narrow exposed substrate material, i.e.,channels, just a few hundred angstrom wide.

d The continuous film stage

The new nuclei formed in the channel area grow and join the large islands, bridging between the elongated islands and eventually filling the channels completely.

2.5 Diffusion of thin films

a The diffusion mechanism

Diffusion usually involves one or more mechanisms depending on the structural defects of the material. The following are the mechanisms of diffusion.

1 Vacancy mechanism

This is the most common type of diffusion mechanism. In thermodynamic equilibrium a certain number of vacant lattice sites can be expected to be present in a crystal. Any atoms neighboring on a vacancy can then diffuse by jumping into the vacancy, the result being an interchange of position of an atom and the vacancy.

2 Interstitial mechanism (Direct interstitial mechanism)

An interstitial atom diffuses by moving directly from one interstitial site without causing net motion of any other atom.

3 Interstitialcy mechanism (Indirect interstitial mechanism)

The interstitial atom moves by pushing a normal lattice atom into an interstitial site and moving into the lattice site itself. The location of the interstitialcy moves twice as far as do either of the individual atoms.

4 Exchange mechanism

Two atoms in the lattice move simultaneously by exchanging places with one another.

5 Divacancy mechanism

Pairs of vacancies that are bound together as divacancies move causing diffusion.

6 Crowdion mechanism

When an interstitial atom is located at a site along a close packed direction the lattice defect, called a crowdion, is generated and an indirect interstitial diffusion mechanism can occur.

7 Relaxation diffusion mechanism

Liquid-like disodered regions where atoms are not really bound to lattice sites may be generated in the neighborhood of a vacancy. Atoms located in this region can move through the crystal.

8 Ring diffusion mechanism

Three or more atoms jump simultaneously to the next site around a ring.

2.6 Thermal diffusion

Because of thermal energy, the atoms in a metal crystal are in constant motion around the equilibrium lattice sites. Occasionally, an atom will jump to a neighboring site. The jump frequency increases as temperature increases. The probability of surmounting the energy barrier, which atoms must overcome to move to the next site, increases as temperature increases causing diffusion. A summary of diffusion theory based on the atomic jump will be presented in the following. The two dimensional diffusion equation is given by,

$$J = -D^* \, dc/dx + V_F \, c \quad \text{----------(2-10)}$$

where

J ; the flux of the diffusing species

D^* ; the tracer diffusion coefficient

c ; concentration of the diffusing species

dc/dx ; concentration gradient

V_F ; the atomic drift velocity from driving forces acting on the atoms

The tracer diffusion coefficient, D^*, and the atomic drift velocity V_F is directly related to the jump frequencies of the atoms. The atomic concentration for the two lattice plane is assumed to be n1 and n2. The frequency of the jump from plane 1 is f12 and from plane 2 is f21. The total flux of diffusion is given by,

$$J = n1 \, f12 - n2 \, f21 \quad \text{---------(2-11)}$$

The local concentration per unit area n is given by,

$$n = c \, a \quad \text{---------(2-12)}$$

where

c ; concentration of the diffusing species

a ; the distance between two lattice planes

The local gradient in the concentration per unit area along the diffusion is given by,

$$dn/dx = (n2 - n1)/a \quad \text{----------(2-13)}$$

From equation (2-10),(2-12) and (2-13), we can derive the following,

$$D^* = a^2 f$$

$$V_F = a\,(f12 - f21) \quad \text{----------(2-14)}$$

where

$f = (f12 + f21)/2$ average jump frequency

The tracer diffusion coefficient is proportional to the average jump frequency while the atomic drift velocity is proportional to the difference of the jump frequencies. Experimentally it is well known that the most important variables which affect D^* are temperature, pressure and chemical composition. For practical purposes , the diffusion coefficient is written with the conditions of constant pressure and chemical composition as follows ;

$$D^* = Do \exp(-E/kT) \quad \text{----------(2-15)}$$

where

Do ; experimentally determined constant for each diffusion couple

E ; activation energy

k ; Boltzmann's constant

T ; temperature

If the energy barrier height is not constant along the diffusion direction , the jump frequencies of the neighboring plane will not be the same and eventually the difference of the jump frequencies contributes to the atomic migration. The difference of the jump frequencies can be caused by the presence of one or more of the following : electric field, temperature gradient, non-ideal part of chemical potential gradient, centrifugal force from angular velocity or stress field.

CHAPTER 3

LOW ENERGY ION BEAM DEPOSITION SYSTEM

The low energy ion beam deposition system was designed and built by P. Bryce , J. Amano and R.P.W. Lawson in 1972 for ion beam studies and since then slight modifications of the electronics system were carried out. The system specifications satisfy the basic requirements for high purity film deposition, which can be summurized as :

a : low pressure in the substrate chamber;

b : controllable deposition rate;

c : readily adjustable final energy of arriving beam;

d : minimum space charge expansion of the ion beam;

3.1 Vacuum system

The vacuum system consists of three interconnected chambers ; ion source chamber,ion beam chamber and substrate chamber. The normal operating pressure of each chamber is ; 1×10^{-3} torr in the source chamber, 1×10^{-7} torr in the ion beam chamber and 1×10^{-8} torr in the substrate chamber. These pressure differences are realized through a differential pumping system. Figure 3-1 shows a schematic diagram of the differential pumping system. The calculated values for the

vacuum system are given by (*1),

P1 = 1 x 10^{-3} torr, P2 = 1 x 10^{-7} torr, P3 = 1 x 10^{-8} torr,

S1 = 0.4 l/sec, S2 = 100 l/sec, S3 = 900 l/sec,

C1 = 0.1 l/sec, C2 = 18 l/sec

The pumps used in this system are as follows;

For the ion beam chamber

a 6 inch diffusion pump(S = 600 l/sec)

b rotary pump

For the substrate chamber

a turbo molecular pump(S = 70 l/sec)

b Ti-ball sublimation pump(S > 1000 l/sec)

c diffusion pump

d rotary pump

For the ion source chamber

rotary pump ; used only for roughing out

The partial pressure of residual gas in the substrate chamber is monitored by an A.E.I. Minimass residual gas analyser. The overall vacuum system is shown in Figure 3-2.

3.2 Ion beam system

The ion beam system is divided into three sections ; a) ion gun, b) ion beam transporting system, and c) decelerator and substrate holder. The ion gun had been modified from the basic Colutron system by J. Amano so that it can accommodate materials with a higher vaporization temperature. This is

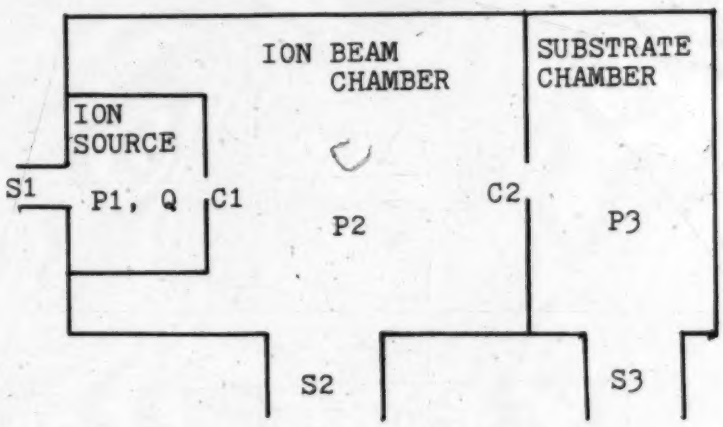

P1 = 10^{-3} Torr
P2 = 10^{-7} Torr
P3 = 10^{-8} Torr

C1, C2 ; Conductance of holes

S1,S2,S3 ; Effective pumping speeds

Figure 3-1
Schematic diagram of differential pumping system

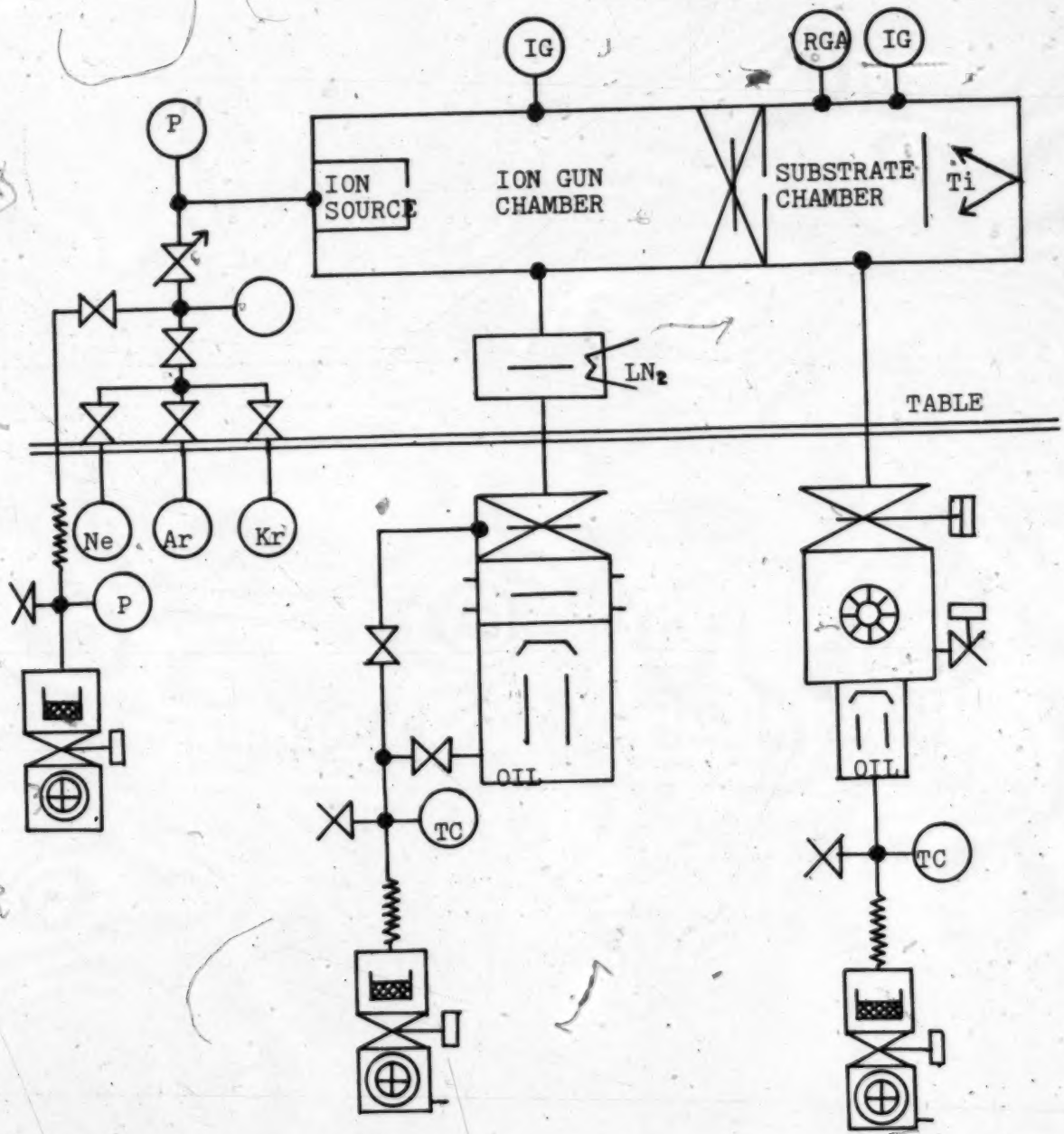

Figure 3-2
Schematic diagram of vacuum system

done by eliminating the problem of condensation between the furnace chamber and the discharge chamber. The schematic diagram of the ion source is shown in Figure 3-3. One of the major parts of the ion beam system is the ion beam transport system. The Colutron ion beam system Model G-2 was chosen for this application. This system consists of an acceleration and focusing system, vertical deflection plates and an E x B velocity filter. Figure 3-4 shows the complete beam system from ion source to target.

The velocity filter consists of a magnet, deflection plates and guard rings. The E field is normal to both the ion beam trajectory and the B field to counterbalance the Lorentz force on a particle of given velocity. Under a balanced condition a selected velocity of ions will pass undeflected through the separator while particles with different velocities will be deflected. Figure 3-5 shows the geometry and mass separation in an E x B separator. In the uniform field region of the separator the motion of an ion will be described as follows when E and B are independent of x or z.

$$m \ddot{x} = e Ex - e \dot{z} By$$

$$m \ddot{z} = e By \dot{x}$$

$$m \ddot{y} = 0 \quad \text{----------(3-1)}$$

By solving the above equations for the balanced condition, i.e., $m \ddot{x} = 0$, $m \ddot{y} = 0$, we get the special velocity Vo,

$$Vo = \dot{z} = Ex / By \quad \text{----------(3-2)}$$

The velocity of an ion entering the velocity filter is

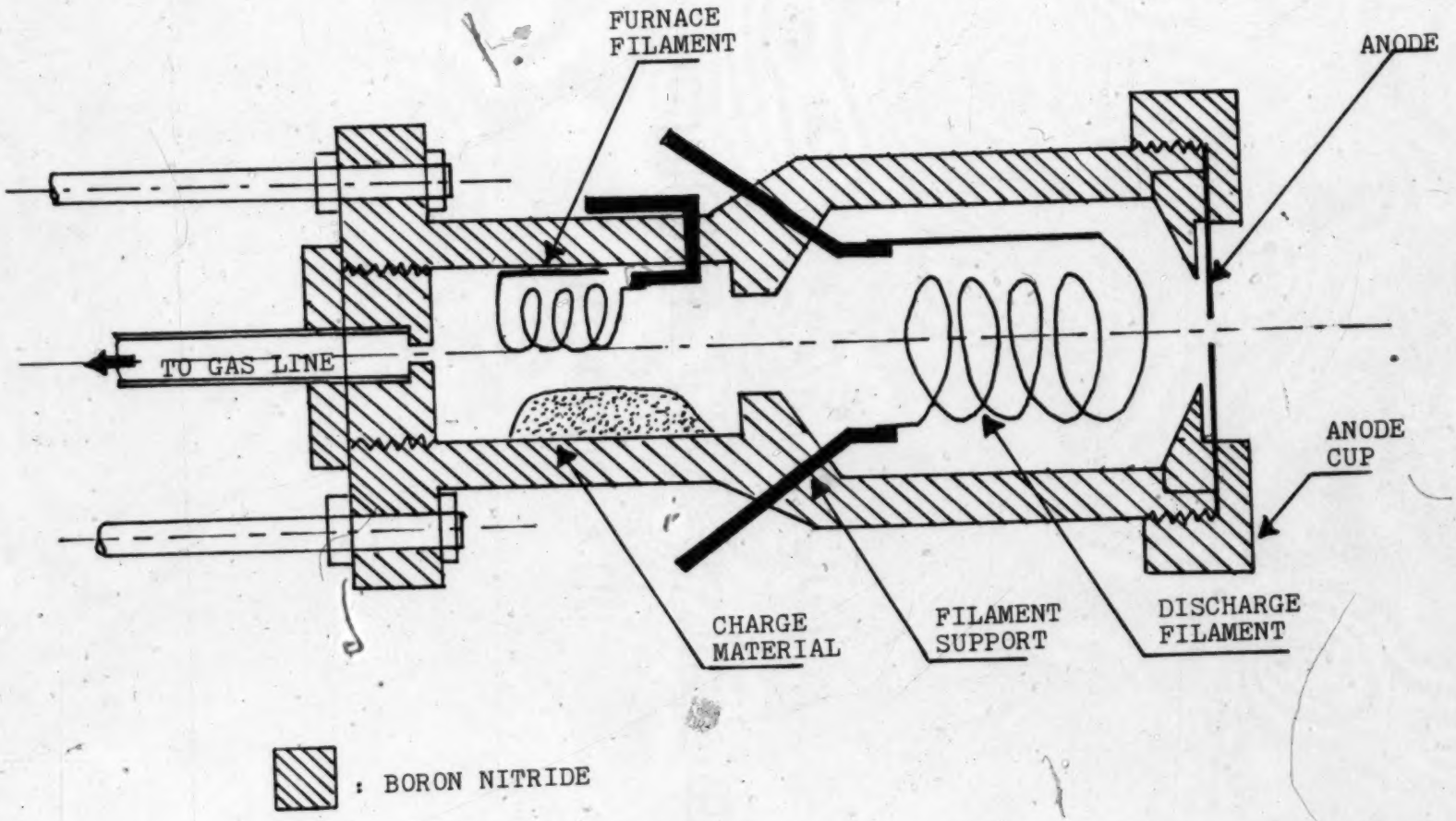

Figure 3-3
Schematic diagram of the ion source

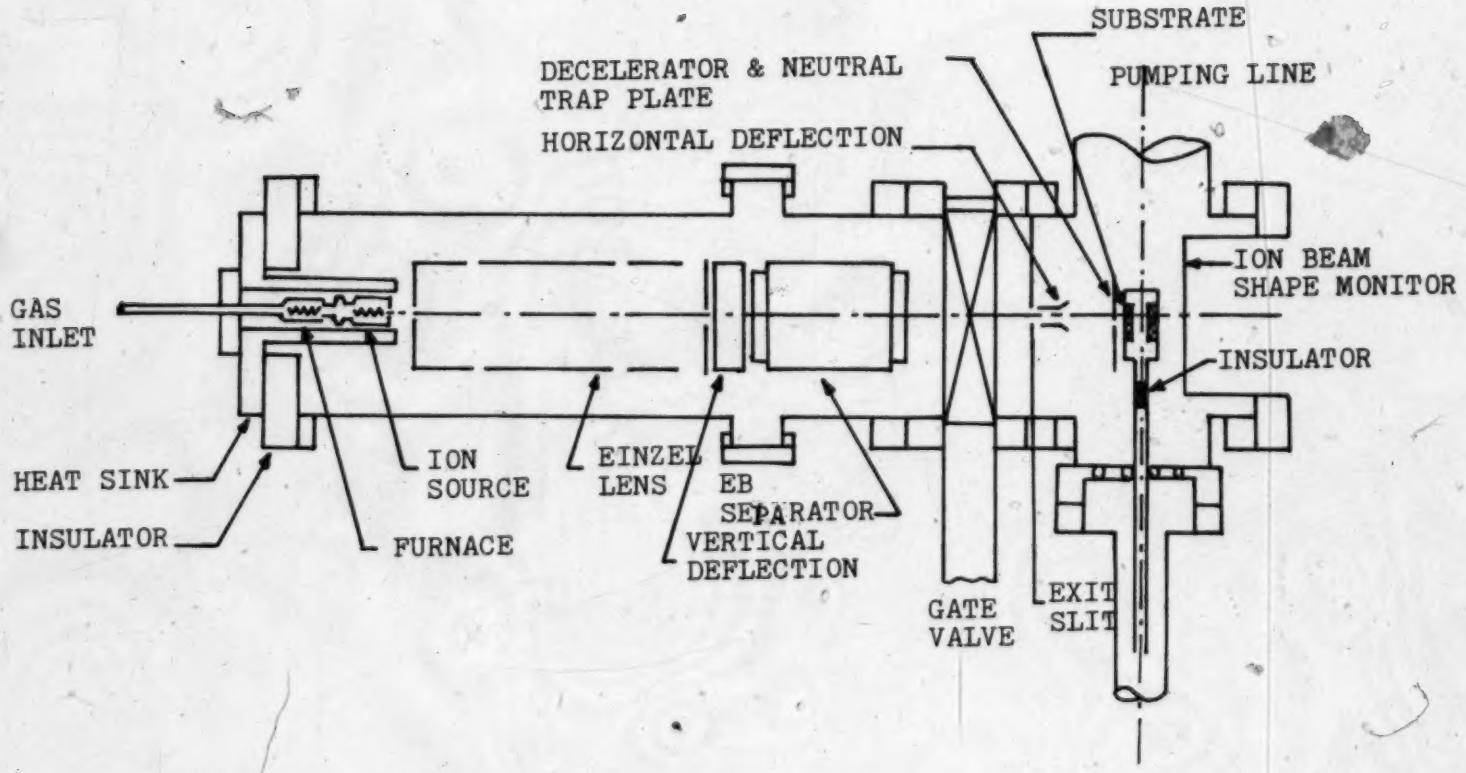

Figure 3-4
Low Energy Ion Beam Deposition System

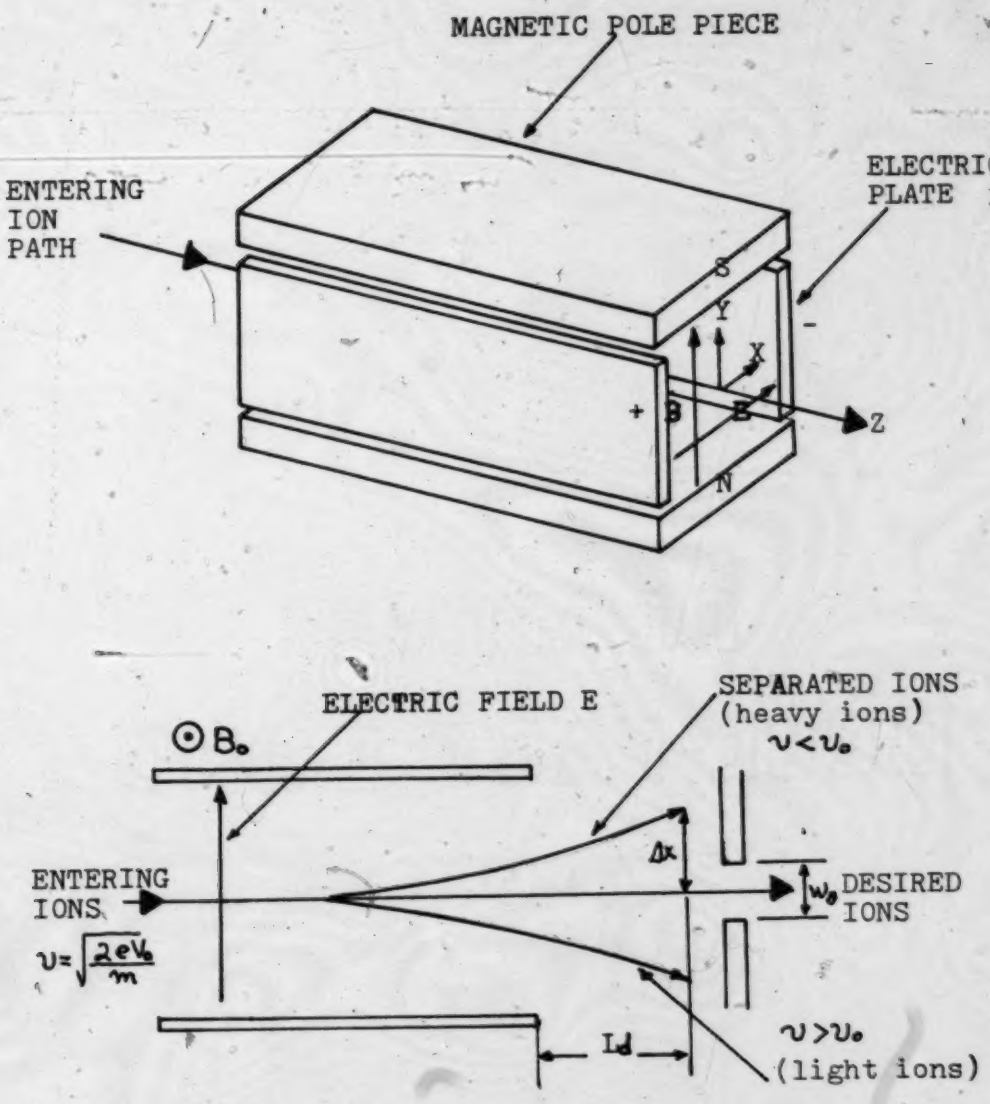

Figure 3-5
Geometry and Mass Separation in ExB Separator

determined by its mass, accelerating energy and ionized charge number. The velocity is given by,

$$v = (2 n e V / M)^{\frac{1}{2}} \text{ ----------} (3\text{-}3)$$

where

M ; mass of ion

V ; accelerating potential

n ; ionized charge number (n=1 for singly charged ion)

e ; electronic charge

The defined mass is selected when the special velocity Vo is adjusted to be equal to v in equation 3-3. During the experiment Ex is fixed to 5.0×10^3 V/m and only By is controlled. It resulted that the overall system mass resolution is $M/\Delta M = 4.5$ and the detectable maximum molecular weight is 600. Also, the velocity filter is used to focus the ion beam into a line image instead of a spot in order to cover a wide area. Equation 3-1 describes only the ideal section of the velocity filter where the E and B field is ideal as shown in Figure 3-5. In fact, the E field is not ideally perpendicular to the Y direction but somewhat barrel shaped, because the E field is generated by a long parallel plate along the z-axis and the spacing between the plates is comparable to plate width. Any distortion caused by this design is corrected by the use of guard rings(Fig. 3-6). A desired ion beam entering the substrate chamber through the exit slit between ion beam chamber and subtrate chamber experiences first of all an electric field for horizontal

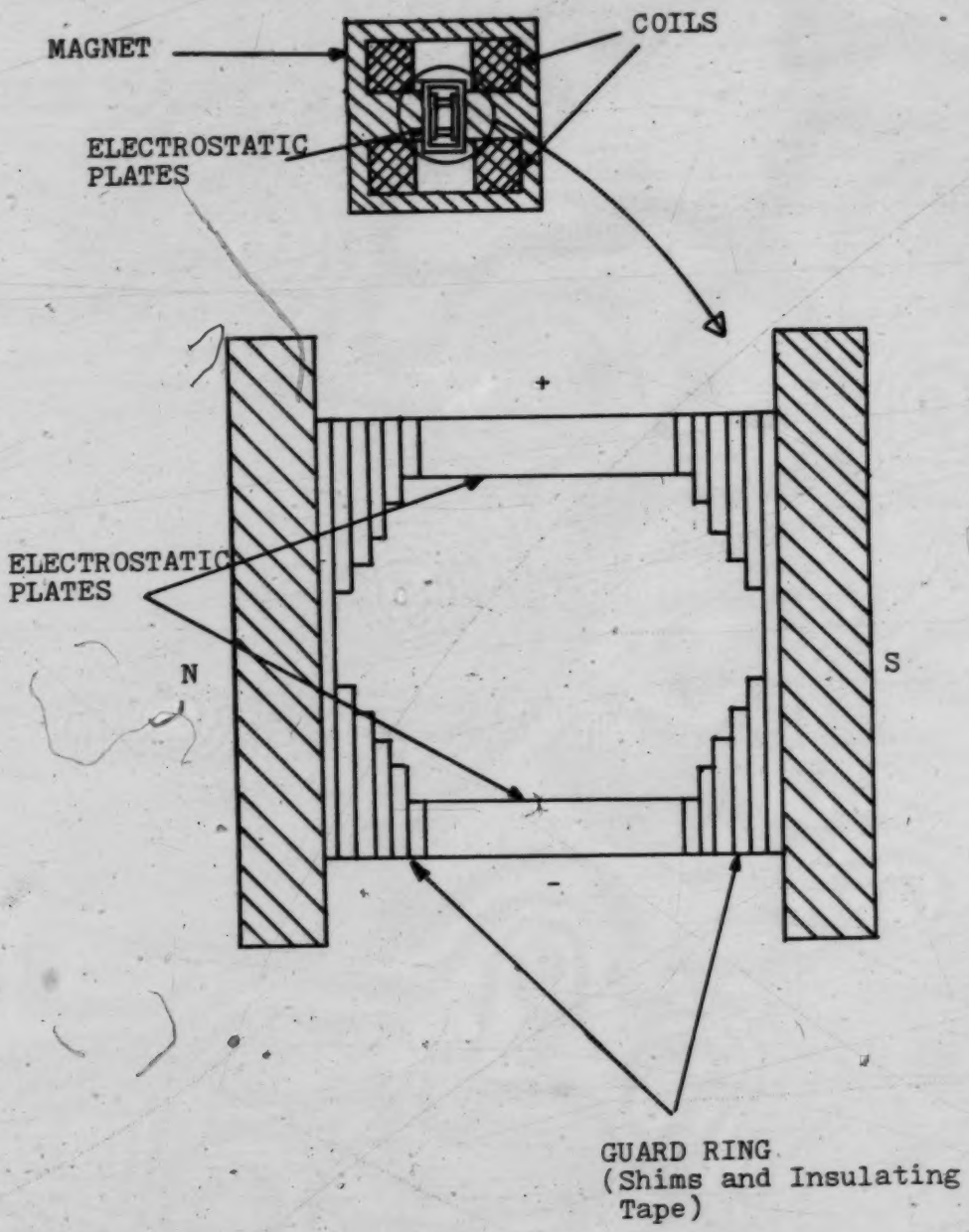

Figure 3-6
Cross Section of Velocity Filter

deflection. The horizontal deflection field and the decelerator(located slightly off the undeflected beam axis) cooperate to eliminate neutral particles that are created during the ion beam transportation process. Figure 3-7 shows this electrode structure. The decelerator plate is located 53 mm from the exit slit and the exit slit is 110 mm from the velocity filter. The mass resolution for the velocity filter is given by (*2),

$$M/\Delta M = a\,l E / (4\,V\,D) \quad \text{---------(3-4)}$$

where

a ; the length of the velocity filter

l ; the distance from the center of the filter to target (drift distance)

E ; the electric field in V/m

V ; acceleration voltage or ion energy

D ; the dispersion between mass M and (M- ΔM)

Applying a=0.15 m, l=250.5 mm, E=5.0 x 10^3 V/m, D=26 mm and we get the mass resolution,

$$M/\Delta M = 4.5$$

With this level of mass resolution, the elimination of Mg isotopes from deposition is not likely to be possible but the detection of isotopes will become possible with a finely focused beam probe. A Van de Graaff accelerator which has He ion beam probe with 1mm diameter will enhance the mass resolution to 5 times and the detection of Mg isotopes becomes possible with this enhanced mass resolution. But the detection of Pb isotopes is not possible even with the

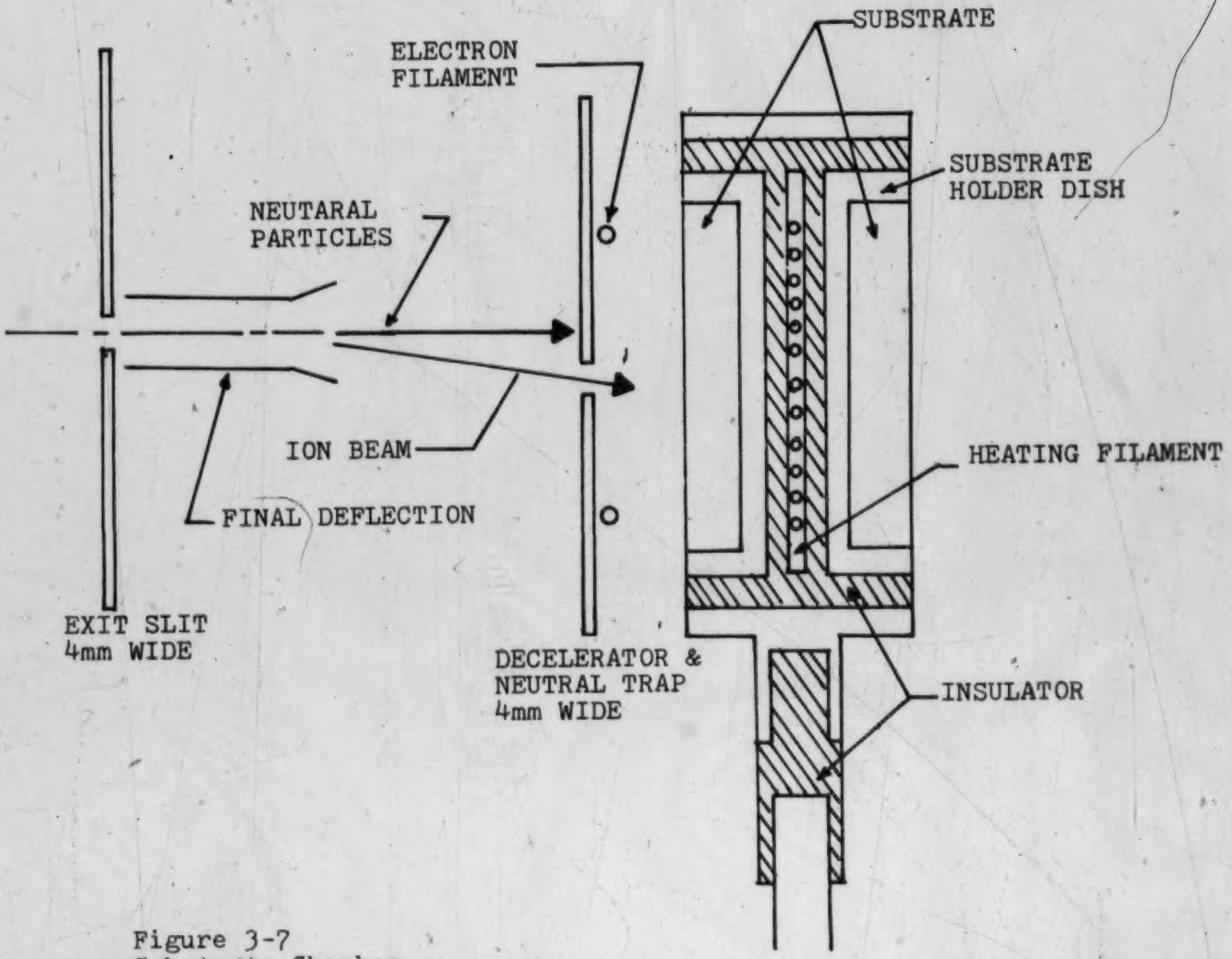

Figure 3-7
Substrate Chamber

enhanced mass resolution. As shown in figure 3-8, the block diagram of system electronics, the whole ion source chamber is floated above ground and kept at a high positive potential (+4 kV). The accelerating electrodes are kept at ground potential. The decelerator plate potential is kept at the same voltage as that of the ion gun. An ion beam energy control power supply is inserted between decelerator plate and substrate with the substrate at the low potential by the amount of desired ion beam energy. Ion beam current on the substrate and decelerator plate are monitored separately and substrate current is integrated to control total charge of deposition.

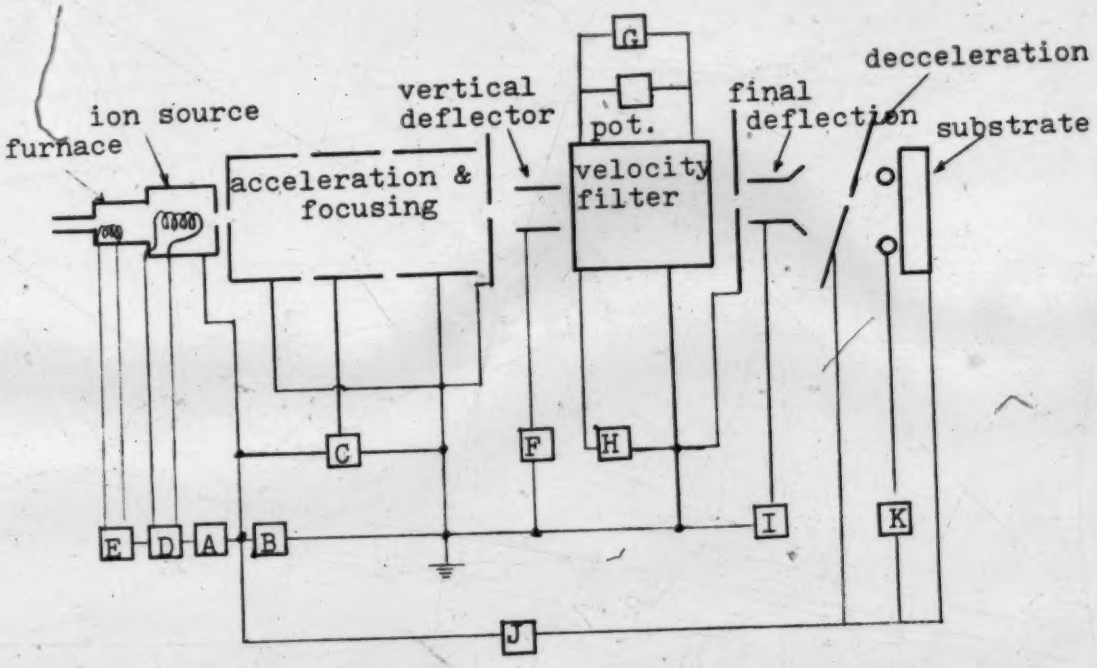

A : Ion source anode power supply
B : Acceleration power supply
C : Einzel lens power supply
D : Ion source filament power supply
E : Ion source furnace power supply
F : Vertical deflection power supply
G : Velocity filter E field power supply
H : Velocity filter magnet power supply
I : Final deflection power supply
J : Ion beam energy power supply
K : Electron filament power supply

Figure 3-8
Block Diagram of System Electronics

CHAPTER 4

RUTHERFORD BACKSCATTERING FOR THIN FILM ANALYSIS

Since E. Rutherford's nuclear scattering experiment was reported in 1911, an extensive range of particle scattering experiments has been studied by scientists. When an energetic particle beam irradiates a target, a fraction of the incident particles will be scattered back from the target by the Coulomb repulsion of the atomic nuclei (Rutherford scattering). The application of Rutherford backscattering to thin film analysis was begun in early 1970 by Chu et. al. (*1,*2,*3) One outstanding feature of this technique is the capability of depth resolution as well as mass, density and composition resolution.

4.1 Mass resolution

The mass resolution arises through the energy loss incurred by the small fraction of incident ions which are backscattered elastically by the Coulomb repulsion of atomic nuclei. The energy of the incident ion after backscattering is smaller than its initial energy Eo by an amount which depends both on the scattering angle and on the mass of the incident ion and a target atom. The relationship is given

by,

$$E = Km\ Eo \quad \text{---------(4-1)}$$

$$Km = (m\cos\theta + (M - m\sin\theta)^{\frac{1}{2}})^2 / (m+M)^2 \quad \text{----------(4-2)}$$

where

E ; the energy of backscattered ion

Eo ; the initial energy of incident ion

Km ; kinematic recoil factor

m ; the mass of incident ion

M ; the mass of target atom

θ ; backscattering angle

Knowing the parameters Eo, m and θ, and measuring the energy of the backscattered primary particle, the mass of an unknown target atom may be found.

4.2 Depth resolution

Most of the incident particles undergo small-angle deflections, penetrating deeper within the target. In the process of penetration, the incident particles lose energy, the backscattered energy of a particle re-emerging from underneath the surface after undergoing a large angle collision is smaller than that from the surface, because of its interactions with target atoms. The energy loss rate of ions in absorbing material is given by(*4),

$$-dE/dx = N\ Z\ (\log 2mv^2/I - \log(1-B^2) - B^2)\ z^2 e^4 / (4\pi\epsilon_o^2\ m\ v^2)$$

where

m,e ;electronic mass and charge

ze,v ; particle charge and velocity

Z ; the atomic number of absorber

N ; the number of atoms /cm^3

I ; the average ionization potential of the ions

B ; the ratio v/c

the negative sign in front of dE/dx signifies an energy loss.

From a trigonometric analysis of Figure 4-1 ;

$E1 = Km\ Eo$

$E2 = Eo - dE/dx\ t$

$E3 = Km\ E2$

$E4 = E3 - dE/dx\ t/\cos\theta$

$= Km(Eo - dE/dx\ t) - dE/dx\ t/\cos\theta$

$= Km\ Eo - dE/dx\ t(Km + 1/\cos\theta)$

Therefore the energy loss ;

$\Delta E = E1 - E4 = (dE/dx\ Km + dE/dx\ 1/\cos\theta)t = (S)\ t$

where

$$(S) = Km\ dE/dx)in + 1/\cos\theta\ dE/dx)out \quad \text{--------(4-4)}$$

(S) is the backscattering energy loss parameter(*5). If we define $(S)_1$ for E =E1 and $(S)_3$ for E =E3, the ratio of $(S)_3$ to $(S)_1$ is given by,

$$(S)_3/(S)_1 = (Km\,dE/dx_{E_o} + 1/\cos\theta\,dE/dx_{E_3})/(Km\,dE/dx_{E_o} + 1/\cos\theta\,dE/dx_{E_1})$$

$$= (Km + 1/\cos\theta\,\epsilon_3/\epsilon_o)/(Km + 1/\cos\theta\,\epsilon_1/\epsilon_o)$$

----------(4-5)

where ϵ_o, ϵ_1 and ϵ_3 are stopping power at energies E_o, E_1 and E_3 from Figure 4-1.

For Mg film, the ratio is calculated by applying the following conditions:

$\theta = 170^{\circ}$, t=5000Å, Kmg=0.5171, E_0=2.0 MeV, E_1=1.0342 MeV, E_3=0.984 MeV, $\epsilon_0 = 45.11 \times 10^{-15}$, $\epsilon_1 = 55.52 \times 10^{-15}$ and $\epsilon_3 = 55.36 \times 10^{-15}$

$(S)_3 / (S)_1 = 0.995$

For Pb film, the given conditions and derived ratios are :

$\theta = 170^{\circ}$, Kpb=0.9262, E_0=2.0 MeV, $\epsilon_0 = 125 \times 10^{-15}$, E_1=1.8524 x10MeV, $\epsilon_1 = 127.7 \times 10^{-15}$,

when t=1000Å,

E_3=1.8142 MeV, $\epsilon_3 = 128.65 \times 10^{-15}$

$(S)_3 / (S)_1 = 1.022$

when t=2000Å,

E_3=1.776 MeV, $\epsilon_3 = 129.14 \times 10^{-15}$

$(S)_3 / (S)_1 = 1.1055$

From the above calculations, it is concluded that (S) can be treated as independent of film thickness with less than 2.5% deviation when the film thickness is less than 5000Å for Mg and 1000Å for Pb. The above results are compatible with the reported deviation of 5% for a 5000Å thickness in SiO (*6).

4.3 Density resolution

When a number of incident particles irradiate the target, only a small fraction of them are backscattered. The possibility of an incident particle being backscattered when passing through the target material depends on the number of

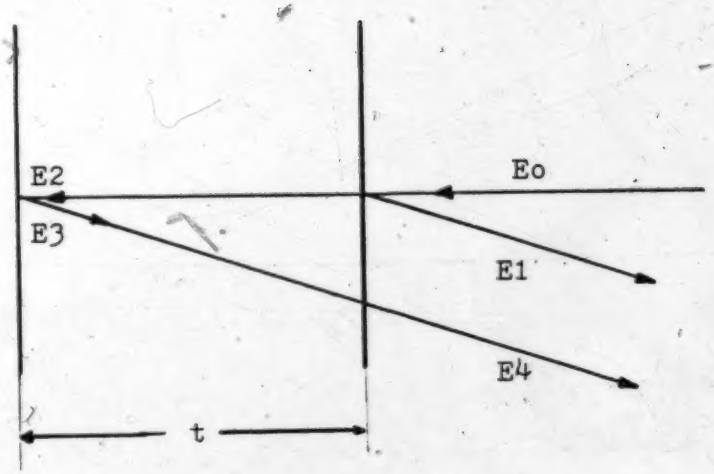

Figure 4-1
Particle energy in the process of backscattering

target atoms per unit volume and the cross section of the target atom. From Figure 4-2, irradiating the target of area a and thickness dx, the total number of backscattered particles N is given by(*7),

$$N = Q/(ze)\,\sigma\,(\bar{N}\rho/A)\,dx \qquad \text{----------(4-6)}$$

where

Q ; the total irradiation dosage of the incident particle in Coulomb

z ; the number of ionization of the incident particle

e ; electronic charge

$Q/(ze)$; the total number of irradiating particles

$\bar{N}$; Avogadro's number

ρ ; density of target material

A ; atomic weight of target material

σ ; total cross section of target atom

From equation 4-6, it is clear that if the density of the target material changes, then the backscattering yield will be changed. In practical cases the backscattering yield measurement is done only for a small solid angle, hence the yield expressed by a differential cross-section, rather than a total cross-section, is more useful. Equation 4-6 then becomes ;

$$N = Q/(ze)\,d\sigma/d\Omega\,(\bar{N}\rho/A)\,dx\,d\Omega \qquad \text{---------(4-7)}$$

And the differential cross-section given by the Rutherford formula is (*7),

$$d\sigma/d\Omega = 1/4\,(e^2 Z1\,Z2/(M1\,V1^2))\,1/\sin^4(\theta/2)$$

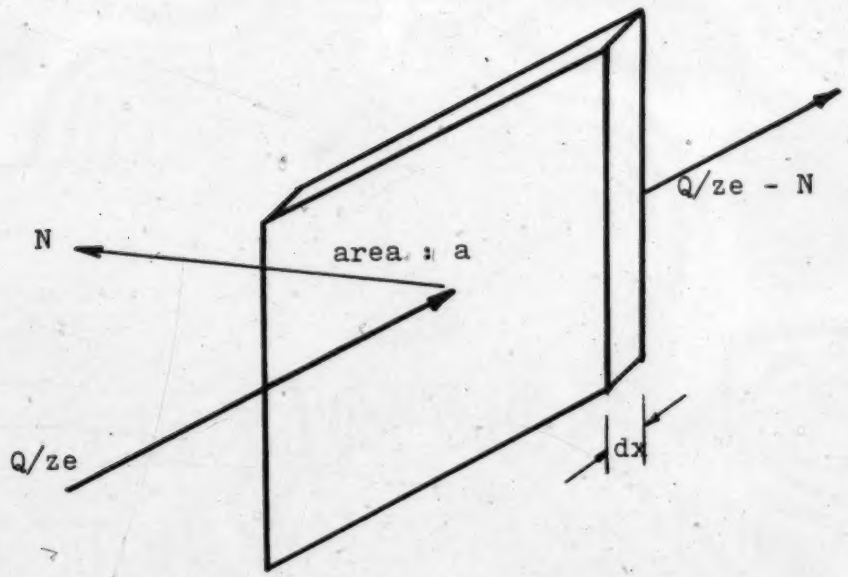

Figure 4-2
Backscattering yield from a slab of target material

----------(4-8)

where

Z1,M1,V1 ; the atomic number, mass and velocity of incident particle

Z2 ; the atomic number of target atom

e ; electronic charge

θ ; backscattering angle

Equation 4-8 is expressed conveniently in terms of energy in MeV, as follows;

$$d\sigma/d\Omega = 1.296 \times 10^{-3} (Z1\ Z2 / E)^2\ 1/\sin^4(\theta/2)\ (b/sr)$$

-----(4-9)

From equation 4-7 and 4-9, the density of the target material can be determined by measuring the film thickness dx and the total number of backscattered particles at given Q, Ω and E.

4.4 Composition resolution

Composition ratio can be determined directly from RBS spectra. The total counts under each peak are directly related to equation 4-7. The ratio of the areas under two peaks is as follows ;

$$N1 / N2 = (d\sigma1 /d\Omega\ \bar{N}\rho1 /A1)/(d\sigma2 /d\Omega\ \bar{N}\rho2 /A2)$$

The ratio of the number of atoms in a unit volume is,

$$(\bar{N}\rho1 /A1) / (\bar{N}\rho2 /A2)$$

$$= (N1/(d\sigma1 /d\Omega)) / (N2/(d\sigma2 /d\Omega))$$

$$= (N1 /N2)\ (Z2/Z1)^2$$ ----------(4-11)

N1,N2 is the total count under each peak. From 4-11, measuring the area under each peak from the spectra, the ratio of the number of atoms is defined. In practical cases, the spectra is divided into certain energy steps. The backscattered particles that fall in an energy step are recorded as the number of counts in that channel, Then the number of counts in one channel is,

$$Hm = Q/(ze)\ d\sigma/d\Omega\ (\bar{N}\rho/A)\,d\Omega\ \Delta x$$

$$= Q/(ze)\ d\sigma/d\Omega\ (\bar{N}\rho/A)\ d\Omega\ \Delta E/(S) \quad \text{------(4-12)}$$

where (S) is backscattering energy loss parameter given in equation 4-4 and E is the energy width of the channel. In a similar way, the ratio of the number of atoms in a compound is defined by the ratio of the number of counts in the peak channel as follows,

$$(\bar{N}\rho 1/A1)/(\bar{N}\rho 2/A2) = (Hm1/Hm2)\ (Z2/Z1)^2\ (\Delta E2/\Delta E1) \quad \text{---------(4-13)}$$

The energy widths of each channel are all the same ; $\Delta E1 = \Delta E2$

therefore, $N1/N2 = (Hm1/Hm2)\,(Z2/Z1)^2$ --------(4-14)

N1,N2 is the number of atoms of composition 1 and 2 in unit volume. Equations 4-11 and 4-14 are valid only if composition is homogeneous along the incident particle passage. If the composition is inhomogeneous and the composition ratio is changing from one dominant element to another without clear boundary regions(like the interface of two films diffused into each other) special consideration for the calculation of the composition ratio is required.

4.5 Composition analysis of multilayer thin film

It is very possible that the interface regions of multilayer thin films consist of several elements making a transition region rather than a clear boundary between two films. The transition region may range from several atomic layers to several hundreds of atomic layers depending on the film production method, the treatment after and,or during film production and the film material combination. Within the interface region it is very likely that the composition ratio varies along the depth from one dominant element to another. In the process of the application of RBS thin film analysis techniques to the interface region of a multilayer film, the problem of stopping power and composition ratio calculation is considered. By measuring the film thickness of each of the constituents in a multilayer film, the overall average energy loss parameter (S) can be calculated from the RBS spectra. When a certain depth range within the film contains more than one element and the composition ratio has a gradient along the depth axis, the procedure of finding (S) by measuring thickness is not applicable because the stopping power dE/dx in the compound region is varying all along the depth axis. The stopping power for the multi-element region can be most precisely determined by measuring the energy loss and the film thickness but this is effective only when the composition ratio is constant everywhere in that region. Measuring the composition ratio

in a certain depth increment, the stopping power of each increment slab can be redefined. Redefining dE/dx and composition ratio for each depth increment can be considered as a probable method for determining the composition ratio profile along the depth axis. The whole process of redefining and recalculating dE/dx and composition ratio is done by the help of a computer. It is known that the only way to determine the energy loss parameter (S) when stopping power dE/dx is not available, is to measure the energy loss from the spectrum and the physical film thickness t (*8). The determination of (S) for an arbitrarily combined compound of 3 or 4 elements by the above method is not suitable for composition analysis because the measured (S) represents the overall average value of the measured thickness, which is usually measured from one side of the film to the other. This problem is somewhat alleviated by employing Bragg's additive rule of stopping power for a compound (*9). Bragg and Kleeman first postulated the linear additivity of atomic stopping power in 1905. Equation 4-14 shows Bragg's additive rule written for a compound made up of three elements x,y,z having a composition ratio n1,n2,n3. The new stopping power for the compound is,

$$\epsilon(x,y,z) = n1\epsilon x + n2\epsilon y + n3\epsilon z \qquad (4\text{-}14)$$

where

$\epsilon(x,y,z)$: the molecular stopping power of the compound.

$\epsilon_x, \epsilon_y, \epsilon_z$: atomic stopping power of x,y,z element. The validity of this equation has been checked by scientists from backscattering experiments. Feng et. al.(*10,*11) showed that the energy loss in Au-Ag mixtures was able to be predicted within 1% accuracy by Bragg's rule and Au-Cu alloys within 2% accuracy, and they proposed Bragg's rule is valid for all metal alloys. They also checked the stopping power of solid oxides and concluded that the stopping power of solid oxygen is 6 - 22 % lower than that of gaseous oxygen. In the process of composition analysis in the following sections of this thesis , the stopping power for solid oxygen is considered to be 85% of that of gaseous oxygen as proposed by Ziegler et. al.(*12,*13).

4.6 Composition analysis applied to Pb-Mg-O-C combination

The atomic concentration profile of a compound of four elements,i.e., Pb,Mg,O,C, is obtained through the following procedure. This procedure, however, is only valid when the spectrum peaks from each element are separated. The RBS spectrum from Pb-Mg-O-C by 2.0 MeV He , gives four, well-separated peaks and it gives one reason why the film materials of Pb, Mg, and the carbon substrate are chosen initially. The definitions of all terms used in this section are given below :

t ; depth in cm(t=0 defines the surface)

Δt ; depth increment

(S) ; backscattering energy loss parameter in eV/cm (see equation 4-5)

dE/dx ; stopping power in eV/cm

ϵ ; stopping power in eV-cm^2/atom

ϵin ; the stopping power in eV-cm^2/atom for particle energy of Ein

ϵout ; the stopping power in eV-cm^2/atom for particle energy of Eout

Ein, Eout ; E for inbound and outbound particle

Hm ; the number of counts in a channel

$d\sigma/d\Omega$; differential cross section in b/sr

subscript 1-4 ; designates element Pb, Mg, O and C respectively

Z ; atomic number

z ; the number of ionization

Q ; the total irradiation dosage of the incident particle

ΔE ; the energy width of one channel

e ; electronic charge

$d\Omega$; the solid angle of detector effective surface measured from target

$\bar{N}$; Avogadro's number

N ; no. of atoms in a unit volume (atomic density)

Km ; kinematic recoil factor

The detailed procedure will be discussed in a later section, a summary follows ;

a. Assume dE/dx for the surface of the film. If the

major elements of the surface are known, assume dE/dx of one of the major elements.

b. Calculate the composition ratio of the surface using dE/dx obtained in step a . The composition ratio will be determined independantly from the error of the dE/dx for the surface assumed in step a.

c. Correct dE/dx for the surface using the composition ratio obtained in step b.

d. Recalculate the composition ratio of the surface using dE/dx obtained in step c.

e. Recorrect dE/dx for the surface using the composition ratio obtained in step d.

f. Increase depth by Δt. Find out the backscattered energies for the each element located at Δt° under surface.

g. Assume dE/dx at the depth Δt is same as that of the surface. Calculate composition ratio at Δt

h. Correct dE/dx at Δt using the result of step f.

i. Increase depth by Δt, now $t=2\ \Delta t$. Go to precedure g and h for $2\ \Delta t$.

j. Continue to increase depth by Δt each time in the same way until the desired depth is reached.

4.6.1 The calculation of composition ratio

The composition analysis from RBS data is discussed by Chu et.al. (*14,*15). It is indicated that the composition ratio obtained from an RBS spectrum is relatively insensitive to the errors involved in the values of stopping power dE/dx used in the calculation (*16). From equation 4-12, the atomic density of each element is given by

$$N1 = Hm1\ (S)1\ K/(d\sigma 1/d\Omega)\ ,\ N2 = Hm2\ (S)2\ K/(d\sigma 2/d\Omega)$$

$$N3 = Hm3\ (S)3\ K/(d\sigma 3/d\Omega)\ ,\ N4 = Hm4\ (S)4\ K/(d\sigma 4/d\Omega) \quad \text{----------(4-15)}$$

$$K = ze/(Q\ \Delta E\ d\Omega)$$

The ratio of N1 through N4 is,

$$N1:N2:N3:N4 = Hm1\ (S)1/(d\sigma 1/d\Omega) : Hm2\ (S)2(d\sigma 2/d\Omega) : Hm3\ (S)3/(d\sigma 3/d\Omega) : Hm4\ (S)4/(d\sigma 4/d\Omega) \quad \text{-----(4-16)}$$

The ratio of differential cross section of each element at the same incident energy is given by equation 4-9 and equation 4-16 becomes,

$$N1:N2:N3:N4 = Hm1\ (S)1/Z1^2 : Hm2\ (S)2/Z2^2 : Hm3\ (S)3/Z3^2 : Hm4\ (S)4/Z4^2 \quad \text{----------(4-17)}$$

(S) is defined by equation 4-4 . It cannot be determined unless the ratio of compound element is found because the term dE/dx of equation 4-5 is indeterminate. Equation 4-5 will be rewritten as,

$$(S) = Km\ N\ \epsilon in + 1/\cos\theta\ N\ \epsilon out$$

$$= \epsilon_{in} N(K_m + 1/\cos\theta \; \epsilon_{out}/\epsilon_{in}) \quad \text{----------(4-18)}$$

Figure 4-3 shows the backscattered energy from different scattering centers in a compound target. The energy loss parameter for each element in the compound is defined from this figure as follows :

$$(S)1 = (E1 - E1')/t$$

$$(S)2 = (E2 - E2')/t$$

$$(S)3 = (E3 - E3')/t$$

$$(S)4 = (E4 - E4')/t$$

Equation 4-18 is extended to a compound of four elements and the energy loss parameter for each element in the compound is given by ;

$$(S)1 = \epsilon_{in} N (K_{m1} + 1/\cos\theta \; \epsilon_{1out}/\epsilon_{in})$$

$$(S)2 = \epsilon_{in} N (K_{m2} + 2/\cos\theta \; \epsilon_{2out}/\epsilon_{in})$$

$$(S)3 = \epsilon_{in} N (K_{m3} + 1/\cos\theta \; \epsilon_{3out}/\epsilon_{in})$$

$$(S)4 = \epsilon_{in} N (K_{m4} + 1/\cos\theta \; \epsilon_{4out}/\epsilon_{in})$$

---------(4-19)

where

Cin : the molecular stopping power of the compound for the particle energy of Eo

Cout : the molecular stopping power of the compound for the particle energy of Kmn Eo

N : the molecular density of the compound

Kmn : the kinematic recoil factor for element n

The ratio of (S)1 and (S)2 is written as,

$$(S)1/(S)2$$

$$= (K_{m1} + 1/\cos\theta \; \epsilon_{1out}/\epsilon_{in}) \; / \; (K_{m2} + 1/\cos\theta \; \epsilon_{2out}/\epsilon_{in})$$

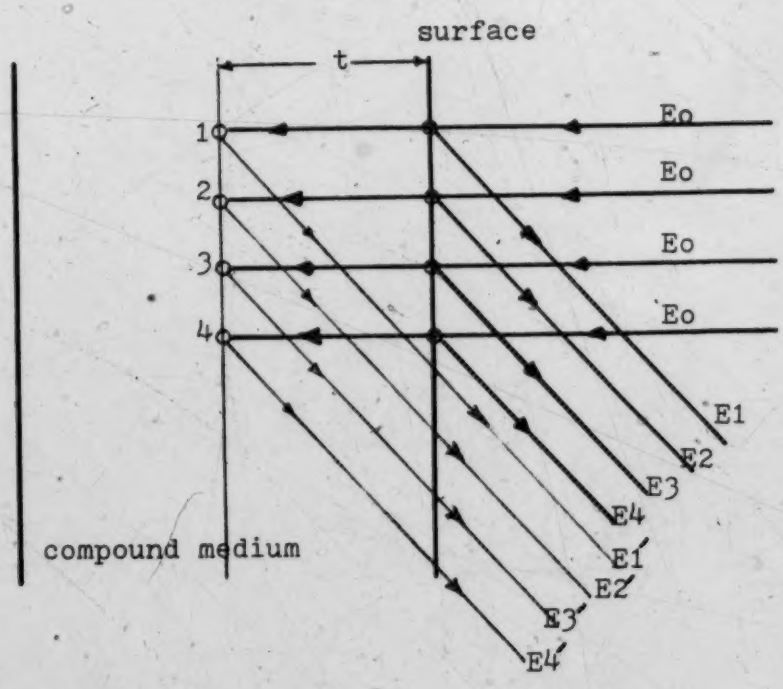

Figure 4-3
Backscattered particle energy from different scattering centers in compound target.

----------(4-20)

From equation 4-20, it is understandable that the ratio of (S) is insensitive to the systematic error of stopping power ϵ. Figure 4-4 shows the stopping power ϵ vs. energy (*17) for the four elements considered in the experiment. When 2.0 Mev He^+ beam is irradiating 5000 Å thick target, the energy range of He^+ and the stopping power range of the target element is also shown and Ein, Eout represent the energy of He^+ in the path of ingoing and outgoing in the target. The energy range of oxygen is calculated by assuming the atomic density of oxygen is the same as that of the molecular density of MgO. The term ϵout/ϵin in equation 4-19 is derivable from Figure 4-4 if the film is not composite. If the film material is composite, a new ϵ vs. energy curve can be drawn for a certain composition ratio of the compound by the help of Bragg's additivity rule and ϵout/ϵin from the composite will be found from the new curve.

4.6.2 Depth prcfile of composition ratio

The stopping power ϵ for the surface of the compound is discussed in the previous section . The backscattering energy loss parameter (S) can be obtained if the atomic density, N, is given. But here we have another diffculty in handling a compound and it is to determine the atomic density N at each depth increment. The atomic density for pure bulk standard material of Pb, Mg, O and C, is given by

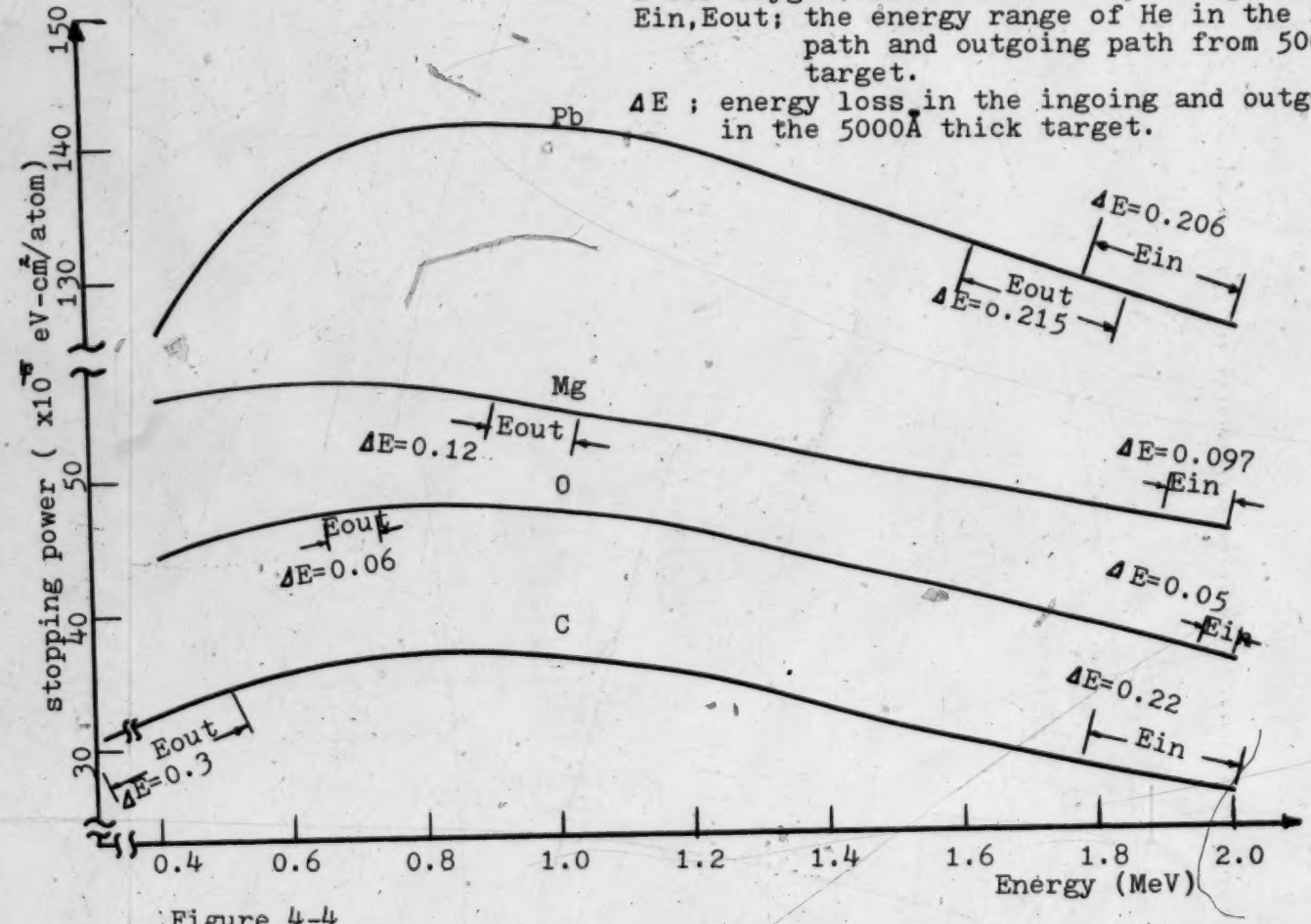

Figure 4-4
He stopping power vs. energy

Table 4-1. Measuring the physical density of a compound, the atomic density can be determined but it is almost impossible to measure the physical density of the arbitrarily combined compounds in the depth scale. The depth profile analysis of an RBS spectrum is done by assuming that N for a pure element with standard density is still applicable when the element contains minor impurities in it. The error involved in the assumption of N will cause an error in the depth scale because the stopping power dE/dx (eV/cm) is given by,

$$dE/dx = N\epsilon \quad \text{---------- (4-21)}$$

But the concentration ratio will not be affected by this error.

Table 4-1

Atomic density for standard bulk material

material	physical density	atomic density (atoms/cm^3)
Pb	11.35	3.3×10^{22}
Mg	1.738	4.3×10^{22}
O		2.67×10^{22} (*1)
C	2.25	11.3×10^{22}

(*1) taken from MgO

CHAPTER 5

EXPERIMENTAL RESULTS AND DISCUSSIONS

5.1 Production of thin film

Both the low energy ion beam deposition and thermal evaporation techniques are employed to produce thin films of Mg and Pb on carbon substrates. During the process of low energy ion beam deposition, the target chamber pressure is maintained below 1 x 10^{-6} torr to avoid possible impurity involvement during film growth. The ion beam is mass and charge filtered to exclude ionized impurities generated by the ion source, and the neutralized or multiply ionized particles from being deposited on the substrate. The selected ion beam energies for film deposition are 24, 48, 72, 121eV for Pb and 24, 48, 100, 150eV for Mg. The combination of these energies makes 32 samples of double layer films of Mg and Pb on carbon substrates. From the RBS spectra of these samples, the most efficient film growth is observed at an energy combination of 48eV for Mg and 48eV for Pb ion beams in both film structures of carbon-Mg-Pb and carbon-Pb-Mg. (Under constant ion beam deposition dosage of 0.22 Coulomb, maximum film thickness was obtained at the above energy combination) The optimum deposition energy for

double layer film of Mg and Pb is confirmed to be the same as that for single layer films of Pb and Mg. An incident ion beam energy of 48 eV was found to be the optimum for producing thin films of Mg and Pb(*2). The investigation focused mainly on films made at the optimum deposition energy of 48 eV. In addition to the above 32 samples of low energy ion beam deposited double layer films, 4 samples of double layer films of Mg and Pb on carbon substrates were produced by a combination of thermal evaporation and low energy ion beam deposition with ion energy of 48eV. Also, 2 samples of double layer Mg and Pb were thermally evaporated onto carbon substrates. The carbon substrates were all polished mechanically before being installed in the target chamber. The thermally evaporated films of Pb and Mg on carbon substrates were made in a vacuum bell jar kept below 5×10^{-5} torr during deposition. The shapes of the ion beam deposited films were controlled to produce rectangular deposits of 1/4 inch wide and 3/4 inch high. Another deposition was carried out on the top of one deposited film so that the two deposition patterns formed a cross. The center of the cross constituted the double layer film while each end of the bar comprised a single layer film of each material. The total dosage of deposited ions was set to 0.22 Coulomb and the expected thickness was 3700 Å for Pb and 2800 Å for Mg provided that the deposition was made very uniformly over the 1/4 x 3/4 inch rectangular shape, no sputtering occurred and the density of a deposited film was

the same as that of bulk material. In practical cases, the deposition shape changed as the ion beam energy was changed because space charge expansion increased as the ion beam energy decreased causing the deposition pattern to broaden. The film thickness therefore varied from the center area where the thickness was the highest to the boundary area where the thickness was the lowest. It was reported that deposition was negligible at Pb ion beam energies higher than 200eV(*1). For Mg ion beams a self sputtering coefficient of unity was observed at an incident energy of approximately 500 eV. The threshold energy for self-sputtering of Pb and Mg was reported as being approximately 24 eV (*2). If the ion beam energy is below the optimum deposition energy, sputtering yield becomes smaller while space charge expansion becomes larger. If the ion beam energy is above the optimum deposition energy, the former becomes larger while the latter becomes smaller. In the both cases, the film growth rate is reduced. The maximum growth rate is achieved only at the optimum deposition energy, i.e.,at the energy which has balanced sputtering and space charge expansion.

5.2 Van de Graaff accelerator preparation for Rutherford backscattering analysis

A $^4He^+$ beam energy of 2.0 MeV was chosen because that energy is well below the possible resonance energy of low

atomic number elements (oxygen and carbon) involved in the experiment. The maximum stopping power and maximum cross sections are obtained around this energy, giving the best depth resolution. Figure 5-1 shows the RBS data handling system. The RBS spectra collected during the analysis was stored on magnetic tape and transferred to SDS 940 minicomputer for further study. Final depth profile analysis was carried out by computer program written for the University's Amdahl 470 V/6. For backscattered particle detection, an ORTEC silicon surface barrier detector was employed and its specifications are as follows(*3) ;

active area ; 50 mm^2

alpha resolution at 5.5 MeV ; 22 KeV

sensitive depth ; 1000 micron

noise resolution ; 18 KeV

operating bias ; -250 V

Considering the dependence of energy resolution on the root mean square of energy, the energy resolution at 2.0 MeV is 13.3 KeV. The secondary electron emission coefficients from Pb and Mg for 2 0 MeV He irradiation were measured as :

γ Pb = 3.93 (electrons/ion)

γ Mg = 2.25 (electrons/ion)

Figure 5-2 shows the effect of suppressor bias on target current during 2.0 MeV He^+ irradiation for each material. The energy distribution of the secondary electrons ranges from 0 to about 20 eV, with 85% from Pb (and 78% from Mg) having energies below 5 eV. These findings are consistent with

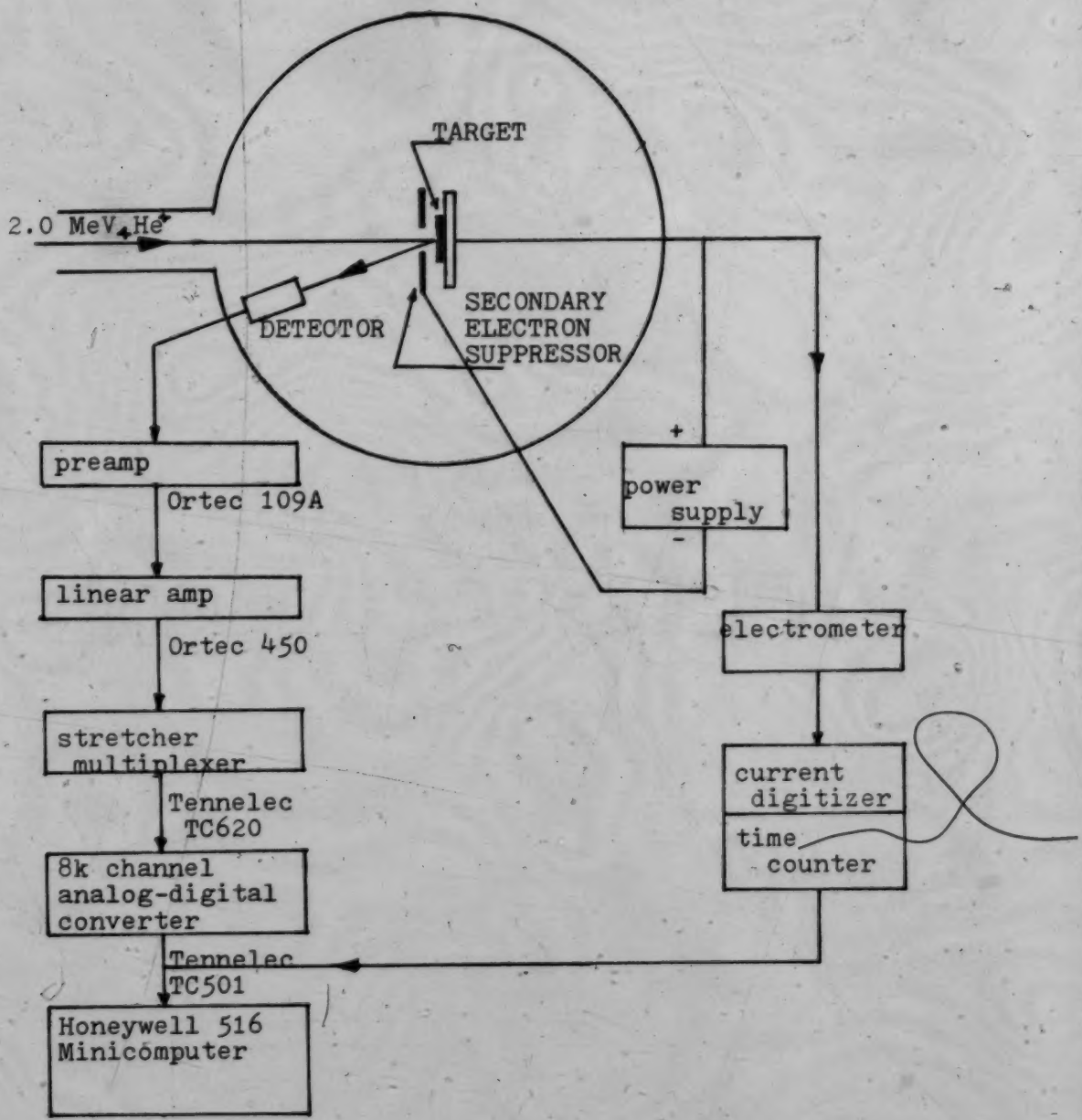

Figure 5-1
RBS Data Handling System

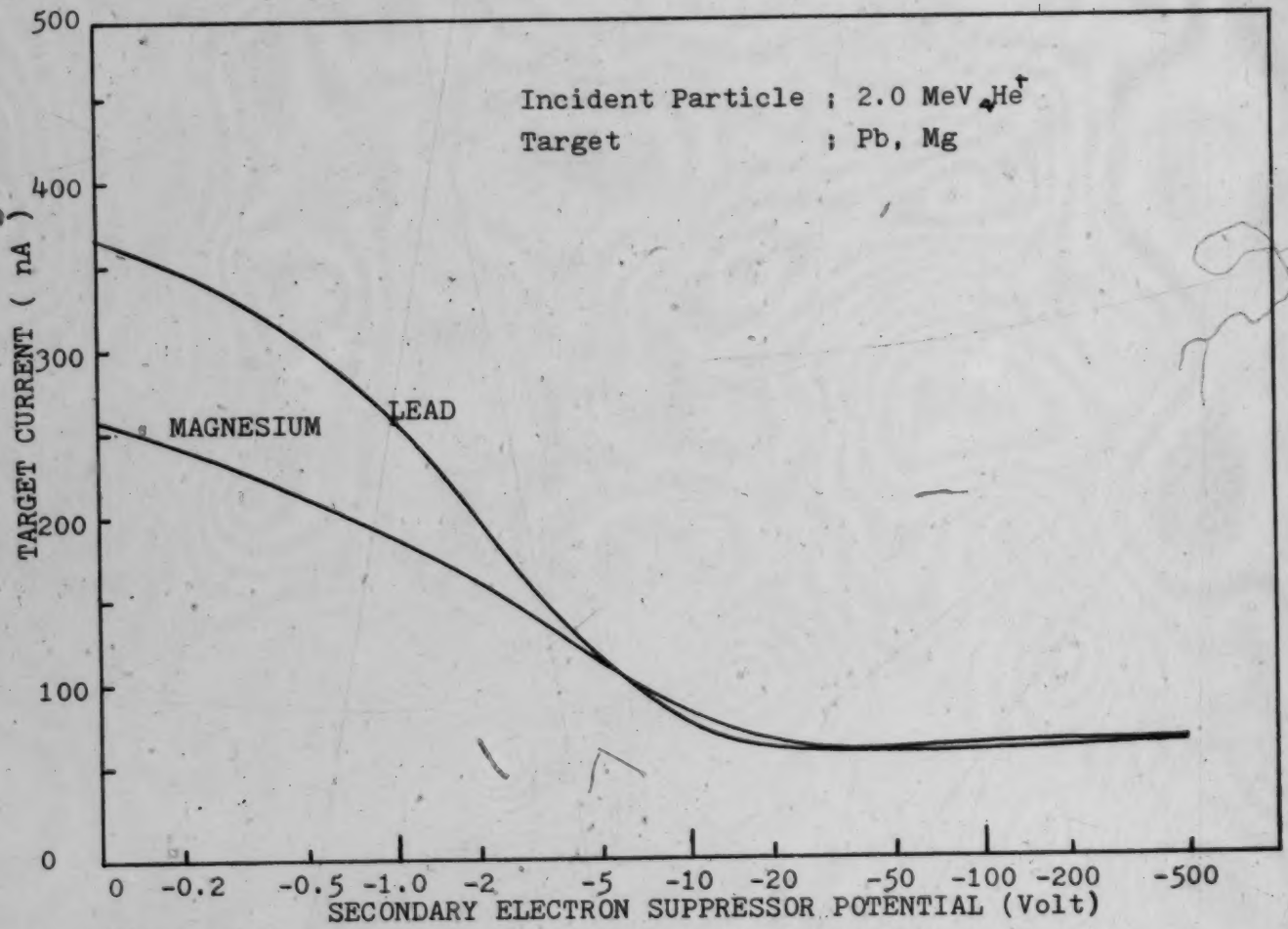

Figure 5-2
Secondary Electron Emission from RBS Target

those of kinetic emission of secondary electrons reported by Kaminsky (*4). The minimum target current is observed when the suppressor bias is between -20 and -50 V. As the suppressor bias is increased to about -100 V, the target current slightly increased and then remained constant beyond a suppressor bias of -100 V. It is postulated that the minimum target current obtained at a bias between -20 and -50 V could infer a maximum energy of secondary electrons lying within this range. Figure 5-3 shows the detector geometry in the target room. ORTEC silicon surface barrier detector is placed at the one end of the cylindrical collimator to increase the directionality of detection. The resulting solid angle of the detector is calculated as 3.25 x 10^{-3} sr. Theoretical backscattering yields of He^{+} from Pb, Mg and C are calculated by equation 4-7 and 4-8. The experimental backscattering yields measured from RBS spectra of Pb, Mg and C are compared with the theoretical values. The ratio of experimental to theoretical is 0.99 for Pb, 1.03 for Mg and 1.04 for C. This result explains that the combined error of He total dosage, detector setting, the applied stopping power and the energy reading from the spectrum is less than 5 %.

5.3 Stopping power and energy straggling data

One of the most important parameters in the analysis of RBS spectra is the correct stopping power data for each

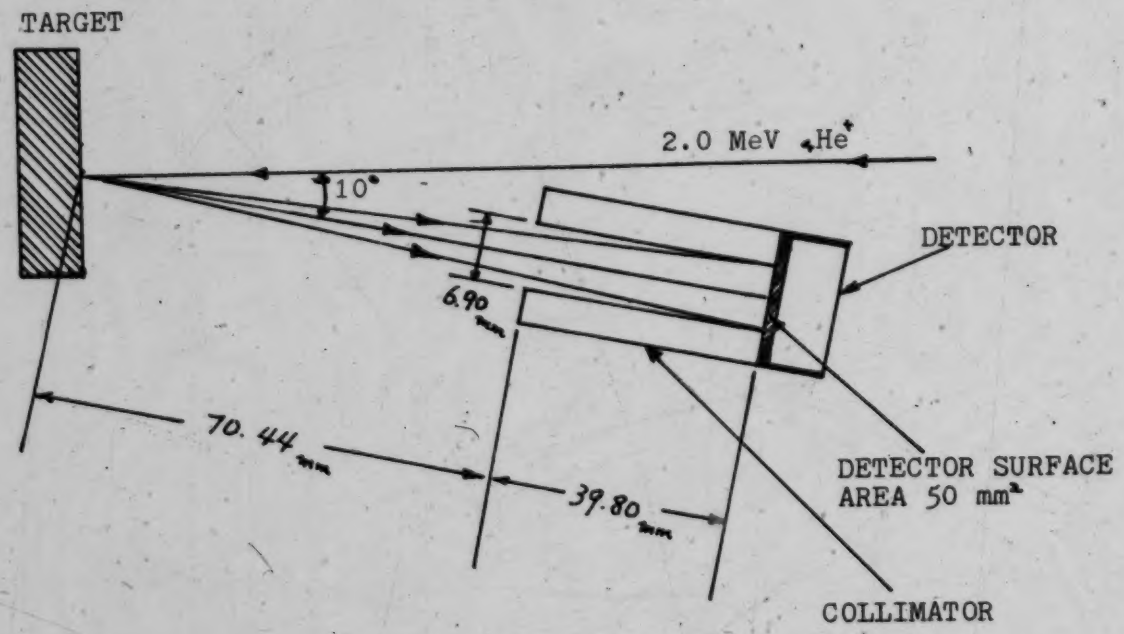

Detector Effective Surface ; 37.4 mm^2
Detector Solid Angle ; 3.25×10^{-3} Sr.

Figure 5-3
RBS Detector Geometry

target element. The stopping power data adopted here are contained in the Atomic Data and Nuclear Data Tables of Ziegler and Chu(*5). The adopted units of stopping power were taken as ϵ (eV-cm^2/atom) unless otherwise specified (e.g. dE/dx (MeV/mm or KeV/Å)). The unit of ϵ is independent of density of the target material and provide a convenient calculation of stopping power of the compound. Table 5-1 shows the stopping power data for alpha particles of between 0.4 MeV - 2.0 MeV energy in Pb, Mg, O and C.

The fluctuation of energy loss when energetic particles penetrate into target material is called energy straggling. The energy straggling theory of Bohr is modified by Lindhard et. al.(*6) ; Chu has calculated energy straggling for He ions in various media using these modified theories. Figure 5-4 shows the energy straggling for Pb and Mg in the backscattering experiment with 2.0 MeV He^+ (*7) . The ingoing and outgoing paths are assumed identical and the ingoing He energy is assumed to be 2.0 MeV. The outgoing He energy is assumed to be 1.8 MeV for Pb and 1.0 MeV for Mg because the approximated kinematic recoil factor for Pb is 0.9 and for Mg is 0.5. The energy straggling for low mass thin film material with less than 5000 Å thickness is not serious compared with the detector resolution(13.3 keV).

5.4 Analysis of Rutherford backscattering spectra

Rutherford backscattering experiments were carried out under

Table 5-1

Stopping power data ($_4He^+$) (*5) (x 10^{-15} eV-cm^2/atom)

energy (MeV)	Pb	Mg	O	C
2.0	125.0	45.11	35.84 (30.46)	25.97
1.8	128.7	46.85	37.91 (32.22)	27.68
1.6	132.4	48.82	40.27 (34.23)	29.72
1.4	135.9	50.99	42.81 (36.39)	31.99
1.2	139.1	53.21	45.29 (38.50)	34.27
1.0	141.6	55.26	47.34 (40.24)	36.19
0.8	141.9	56.78	48.39 (41.13)	37.21
0.6	138.1	57.26	47.72 (40.46)	36.58
0.4	126.4	56.04	44.34 (37.69)	33.32

* the value in parenthesis is for oxides

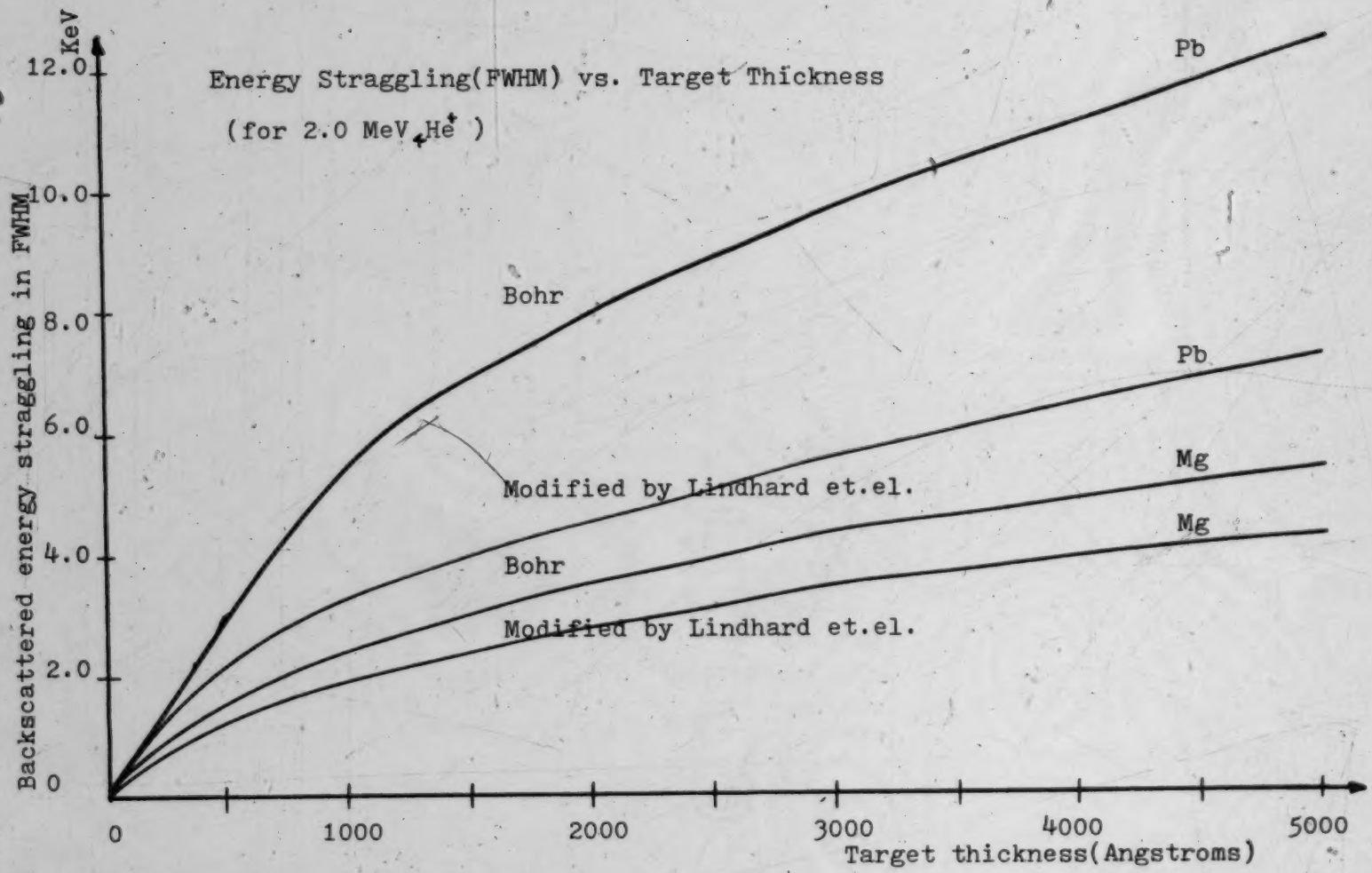

Figure 5-4
Energy straggling in the backscattering experiment of 2.0 MeV $_2He^4$ with target of Pb and Mg. (*5)

the following machine conditions.

a. Ion beam energy : 2.0 MeV He^{+}

b. Secondary electron suppressor bias : -200 V

c. Ion beam current : adjusted in the range of 1×10^{-7} - 1×10^{-9} amp., depending on the target material to avoid piling up of data. normally for Pb 1 - 5 nA, Mg 50 - 100 nA

d. Total ion dosage : 10 - 60 micro Coulombs.

e. Backscattering angle : 170 degree

f. Target annealing and cooling : target holder is heated by an electric heating element imbedded in the target holder. The target chamber pressure is maintained in the range of 10^{-6} torr during annealing. An iron - constantan thermocouple is used to monitor the target temperature. Argon gas is used to cool down the target to room temperature after each annealing

5.4.1 Background level elimination

Initially the backscattering spectrum is recorded into 4096 channels by a Honeywell 516 minicomputer and later the channel numbers are reduced to 1024 by averaging each four channels. Before the spectrum is used as input data for depth and atomic concentration analysis, the background

level should be removed otherwise the background signal would give false input information for the analysis. The background level removal is done by the following peak finding method (*8) :

The initial spectrum is assumed to be Gaussian and the spectrum is smoothed by using a Gaussian weighting function. The Gaussian weighting function has K times larger standard deviation than the initial spectrum. The value of K is empirically determined and in this experiment K=6 is selected. A new spectrum is made by convoluting the initial spectrum with the weighting function and the background free spectrum is obtained by deducting the new spectrum from the initial one. Figure 5-5 shows the procedure of the background level removal.

From Figure 5-5,

A : initial spectrum with background

B : background

S : new spectra obtained by weighting function

D : background free spectra

The new spectrum is given by,

$$Si = \left(\sum_{j=-L}^{L} Wi\ Ak\right) \Big/ \sum_{j=-L}^{L} Wj \quad , \text{ where } k = i+j$$

$$Di = Ai - Si$$

where

Ai : ith data of initial spectrum

Wj : jth data of weighting function , $Wj = w(j) = e^{-j^2/2\sigma_w^2}$

σ_w : the standard deviation of weighting function

s : the standard deviation of the initial spectrum

$\sigma_w = K s$, (where K=6 is chosen in this experiment)

By adjusting the value of K, the elimination level can be adjusted and set to the predicted channel axis zero intercepting point.

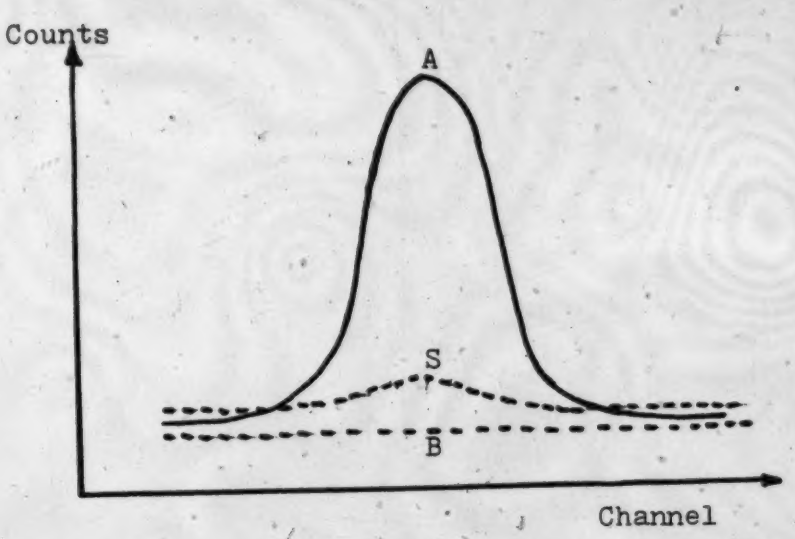

Before background signal is eliminated.

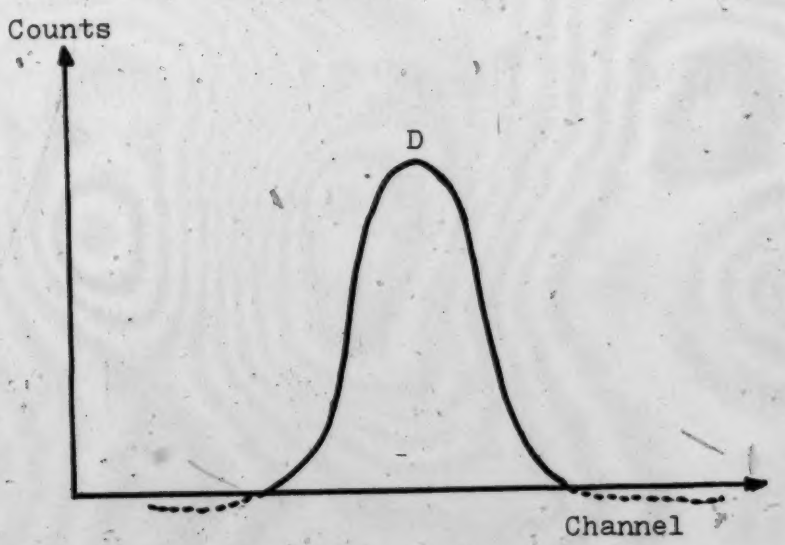

After background signal is eliminated.

Figure 5-5
Background level removal

5.4.2 CM(T) and CM(48)

a. RBS spectrum of magnesium

Figure 5-6 shows a portion of a complete spectrum for magnesium from CM(T) and CM(48). The leading edge of CM(T) lies ahead of CM(48) by about 50 KeV and the half maximum point of the front edge of CM(T) is 28 KeV ahead of CM(48). This energy shift is explained by the isotopes of Mg. Table 5-2 shows the Mg isotopes and their abundance. The calculated value of the energy shift between mass 23.985 and 24.986 is 28.4 KeV ,and between 23.985 and 25.983 is 55 KeV. The thermally evaporated Mg film consists of mass 23.985, 24.986 and 25.983 whilst the low energy ion beam deposited Mg film is made of single mass 23.985.

b. The oxidation of CM(T) and CM(48)

The complete RBS spectra of CM(T) and CM(48) from which figure 5-6 are extracted, show an oxygen peak in both cases. Mg is chemically very reactive with oxygen and unfortunately the ion beam deposited films from the ultra high vacuum chamber have to be transported at atmospheric pressure to the storage bell jar, or to the Van de Graaff for RBS analysis. The oxidation of Mg has

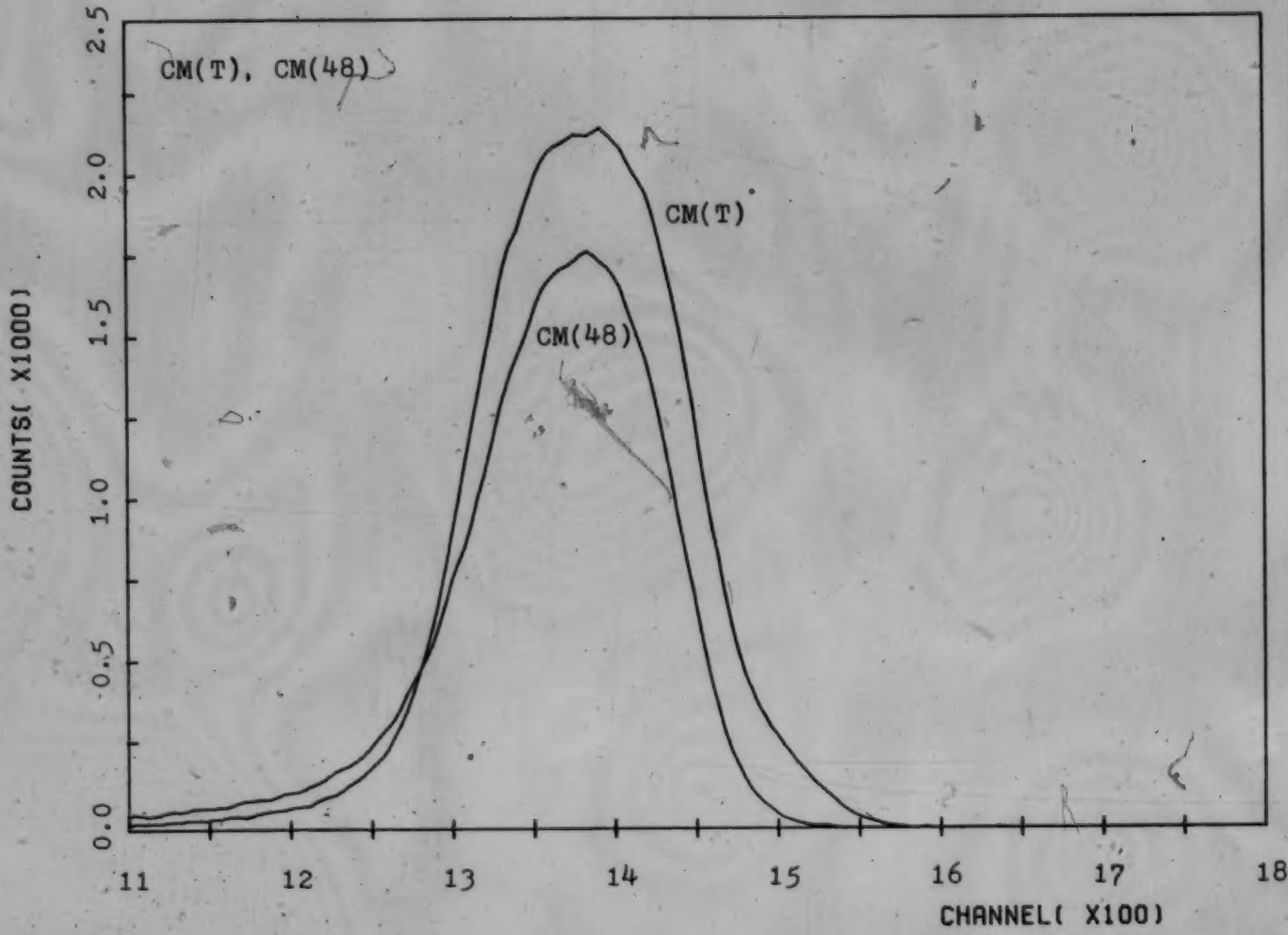

Figure 5-6
RBS spectra of CM(T) and CM(48)

Table 5-2

The isotopes of Mg

mass (amu)	natural abundunce (%)	kinematic recoil factor $\theta = 170^{\circ}$, $^{4}He^{+}$
23.985	78.7	0.5123
24.986	10.1	0.5265
25.983	11.1	0.5398

been investigated by many scientists and the measured oxidation rate of Mg is given in Table 5-3 (*9,*10). If we assume a magnesium oxide layer is formed on the surface of the Mg film and the slab of MgO grows thicker as oxygen is taken up, the oxide layer growth rate can be calculated from the above data. The oxidation rate of Addiss(*9) is equivalent to 2 Å /min. - 4.7 Å /min. and Cohen's(*10) data is equivalent to 0.4 Å /min. - 2.5 Å /min. provided that the magnesium oxide has the standard value of density. According to the above data, the storage of pure Mg films in the vacuum bell jar which has about 10^{-5} - 10^{-6} torr oxygen partial pressure, cannot keep the sample from oxidation beyond several days. The 5000 Å thick Mg film takes only about 30 - 200 hours to be oxidized in the vacuum bell jar at room temperature. Experimental results of the oxidation rate of Mg (*11) show that the sticking probability of oxygen does not drop when thicker oxide is present. This finding is not expected on the basis of the usual concepts of oxide film formation. This phenomenon is explained by Landsberg (*12) who assumes that oxygen is chemisorbed on active sites, which are deactivated, but create at the same time new ones. Figure 5-7 and 5-8 show the derived depth profile

and atomic concentration of CM(T) and CM(48). Landsberg's assumption is very compatible with the oxygen and magnesium concentration profile which shows fresh Mg on the surface and no oxide surface barrier which would block the intake of oxygen. Oxygen is evenly distributed in the Mg region rather than forming a high oxide concentration region in the surface area.

Table 5-3

Oxidation rate of Mg

reference	oxcidation rate (μgm/cm^2 min)	measurement condition	
		temperature (°C)	oxygen pressure (mm Hg)
Addiss (*9)	0.014 - 0.034	400 - 440	25
Cohen (*10)	0.003 - 0.018	room temperature	10^{-7} - 10^{-5}

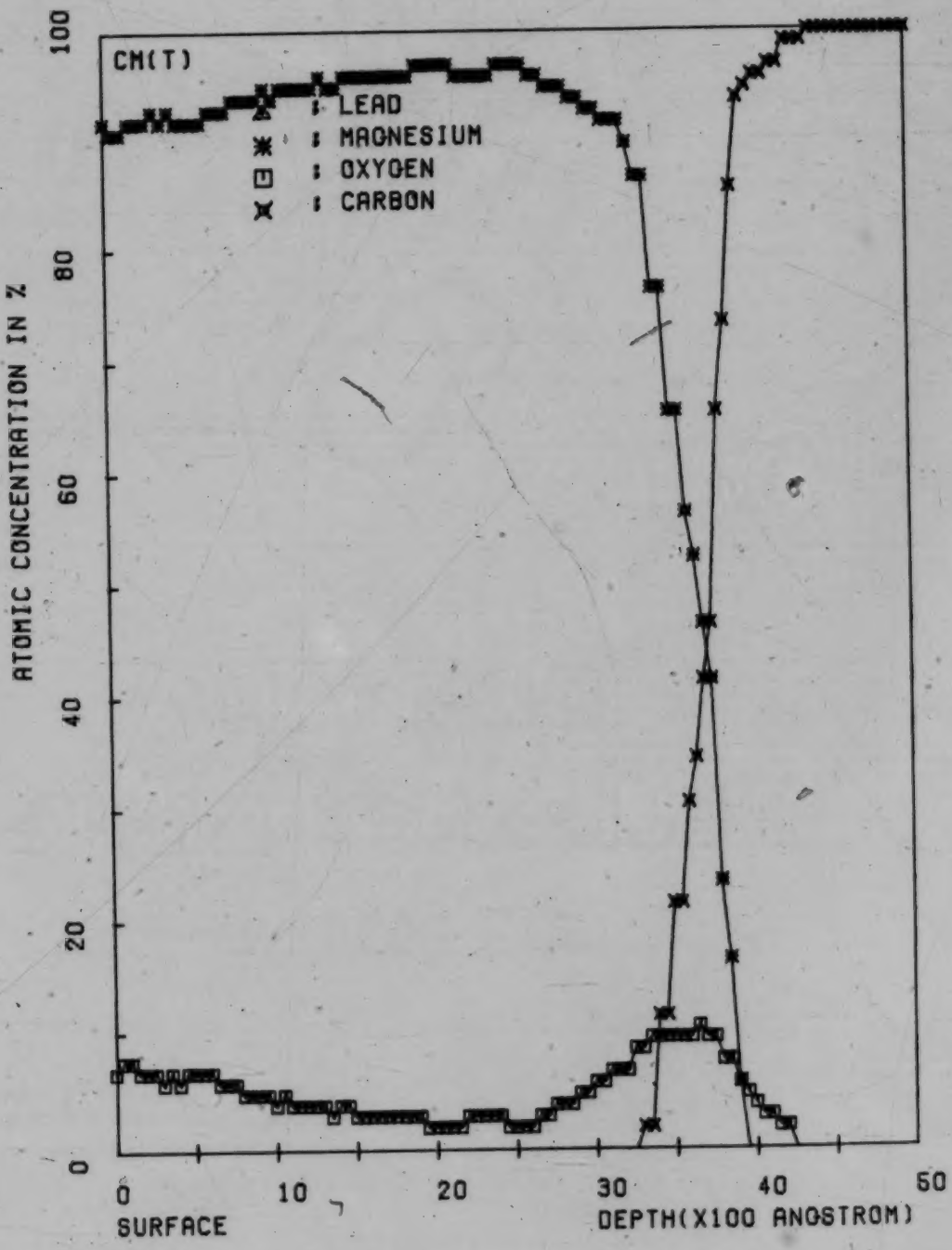

Figure 5-7
Depth profile of CM(T)

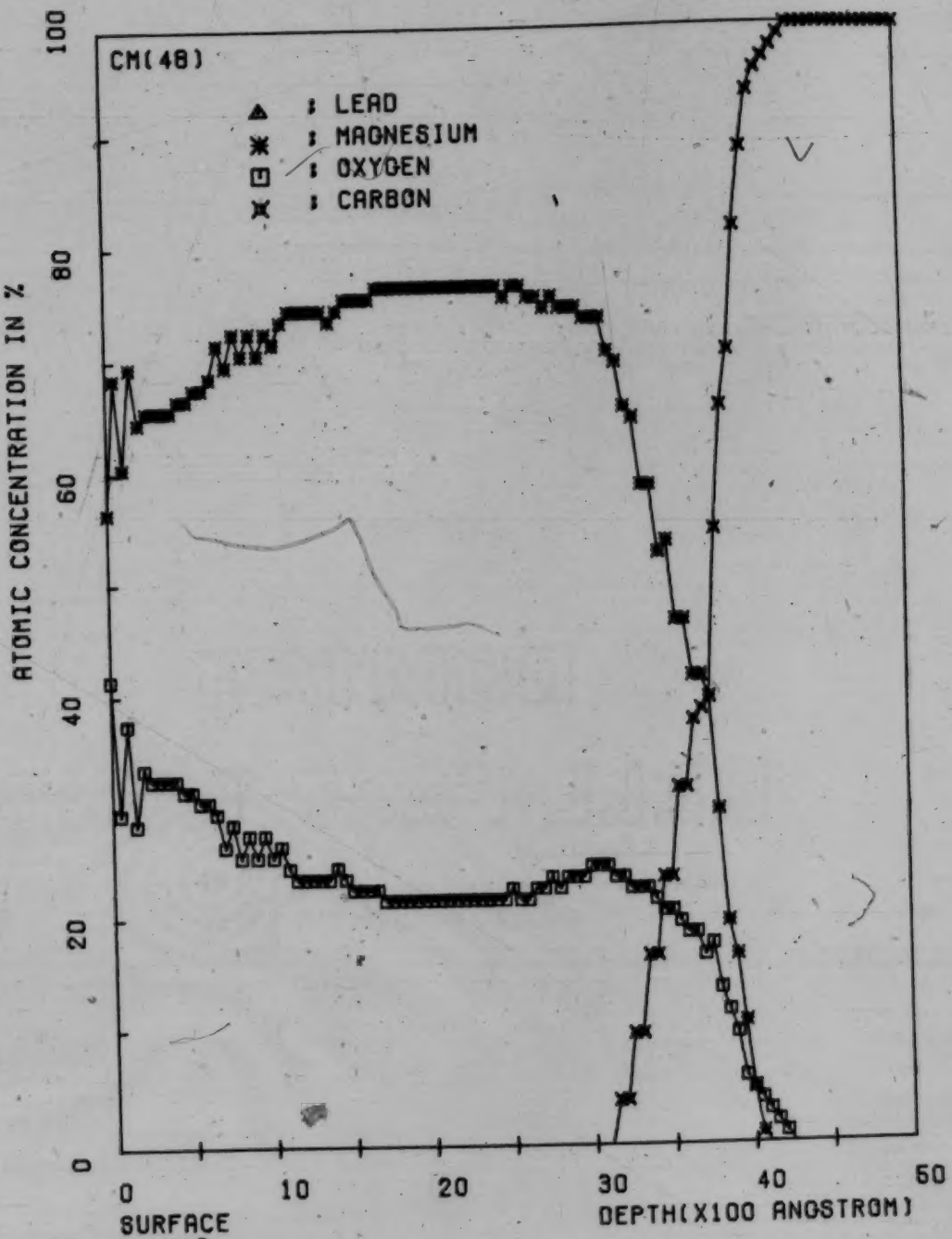

Figure 5-8
Depth profile of CM(48)

5.4.3 CP(48)M(48) and CM(48)P(48)

Figures 5-9 and 5-10 show typical RBS spectra and Figures 5-11, 5-12 show the derived depth profiles of the CM(48)P(48) and CP(48)M(48) film system. From both depth profiles, no sharp interfaces exist between adjacent material. The composite region between the Mg and the Pb layer ranges over 1000 Å wide . The composite region between carbon and Mg or carbon and Pb layer is much narrower than that of the Mg-Pb interface. The penetration of Pb atoms into the Mg layer is more noticeable than that of Mg atoms into the Pb layer. The probability of preferential diffusion of Pb into Mg is seen from the surface topography of both films. Figure 5-13 shows SEM topography of CM(48) and CP(48). The surface of CP(48) shows grains which are much larger than those seen from the surface of CM(48). It is suggested by Shewmon (*16) that the major atomic migration route is via grain boundaries when the temperature is below 0.75 T(melt) K. Campisano et.al. (*14) pointed out that the preferential diffusion direction was controlled as the grain size of the host film and receiving film was altered. The preferential diffusion of the film with larger grain size into the film with smaller grain size is observed and it is explained by a longer grainboundary path

existing in the film having a smaller grain size. The surface topographies of the films illustrate a considerable amount of holes and cracks on the film surface. These holes and cracks are checked by the SEM in the electron probe mode and the characteristic X-ray coming from these holes and cracks do not show any difference from those coming from smoother film areas. The holes and cracks are only on the surface and they do not reach to the bottom layer or substrate. The surface roughness of the film could be due to the surface roughness of the carbon substrate. Figure 5-14 shows the surface topography of carbon substrate.

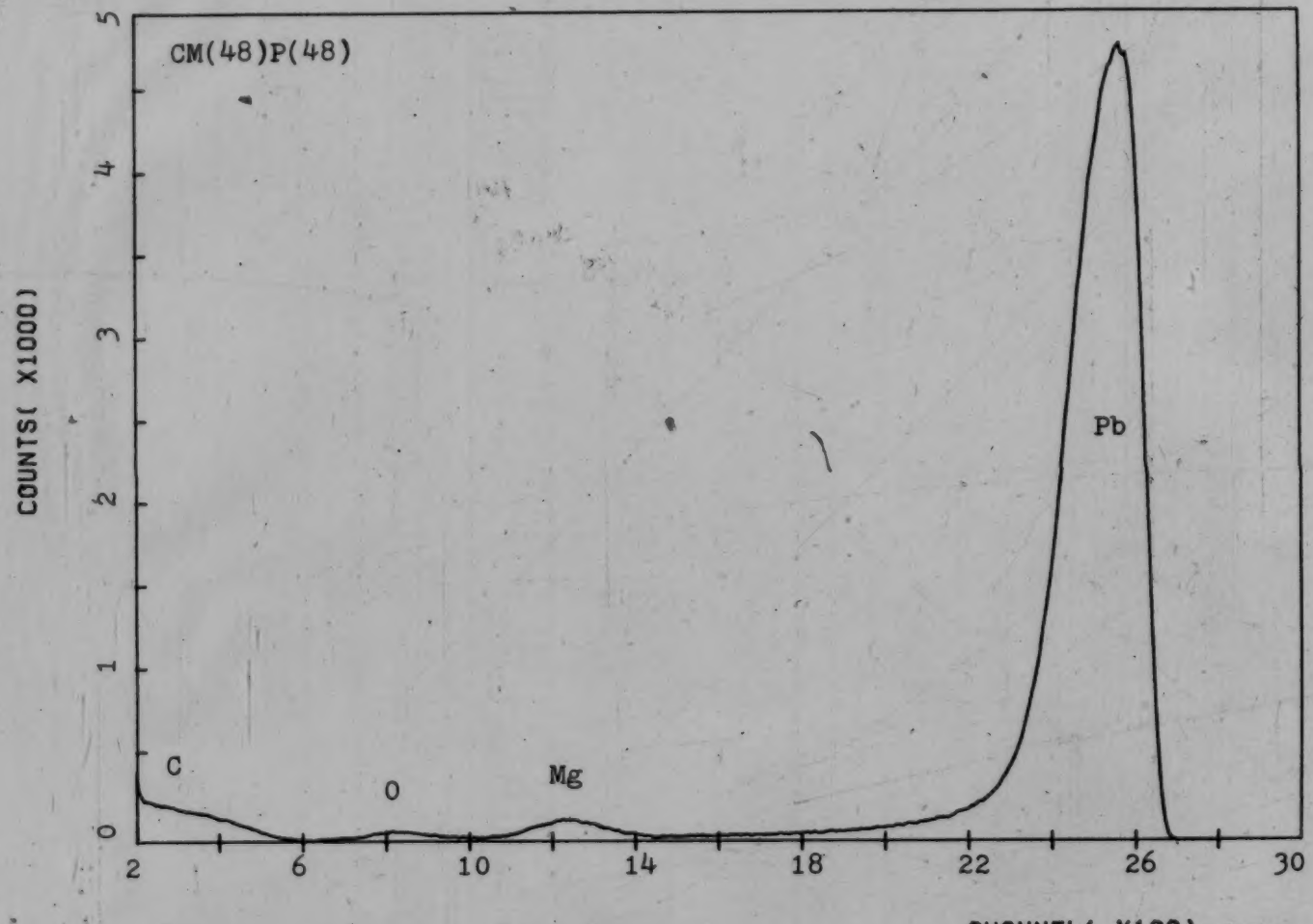

Figure 5-9
RBS spectra of CM(48)P(48)

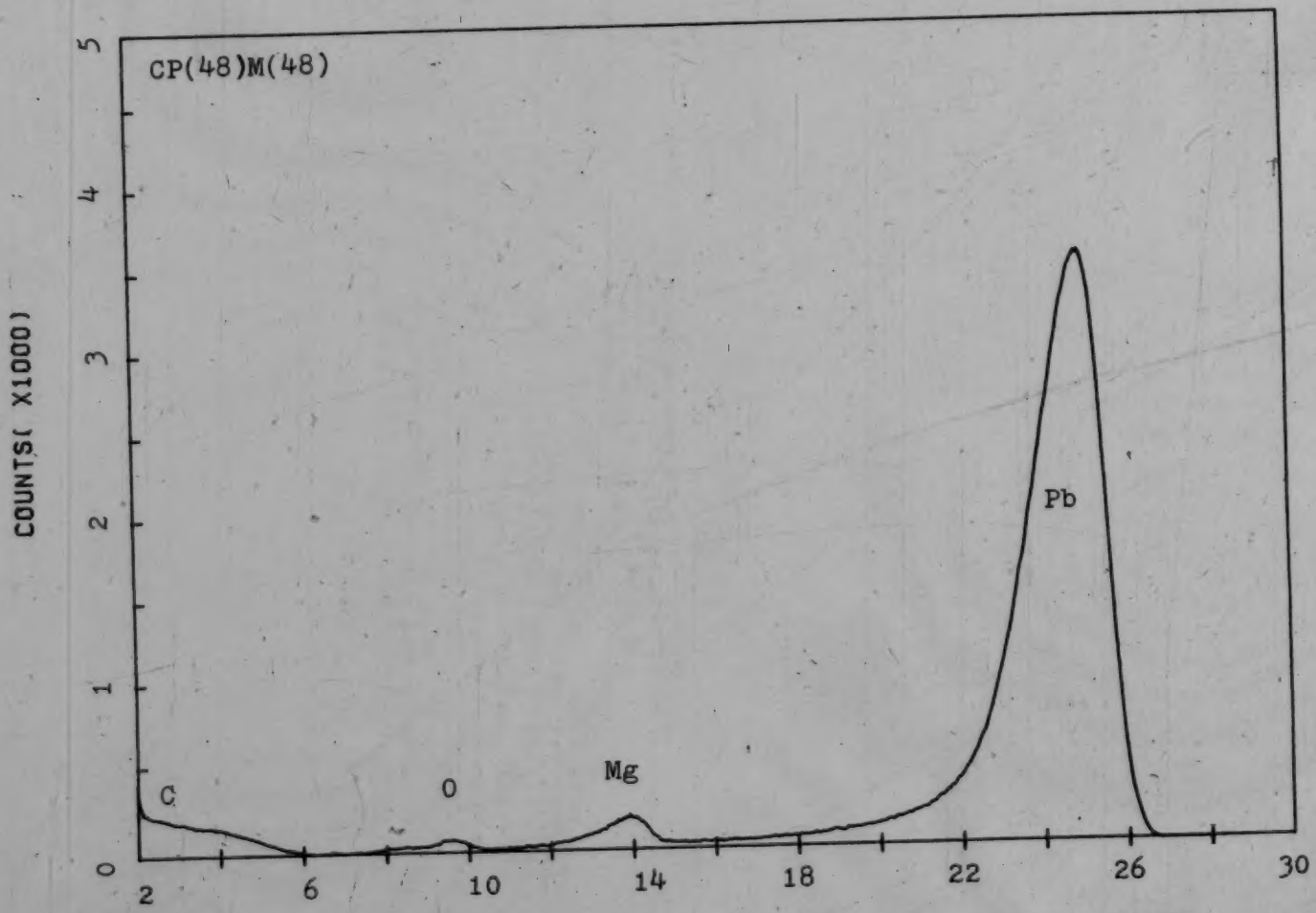

Figure 5-10
RBS spectra of CP(48)M(48)

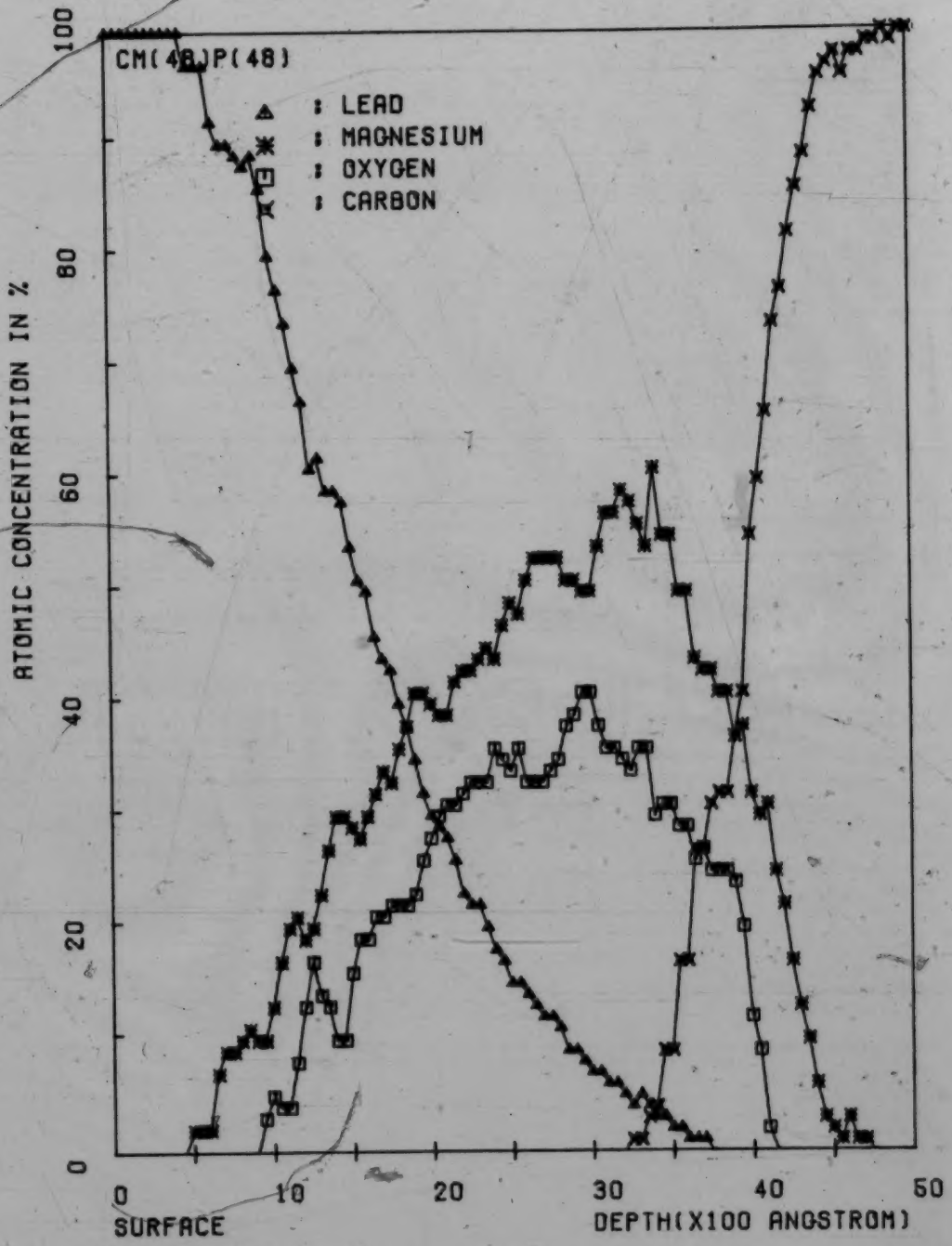

Figure 5-11
Depth profile of CM(48)P(48)

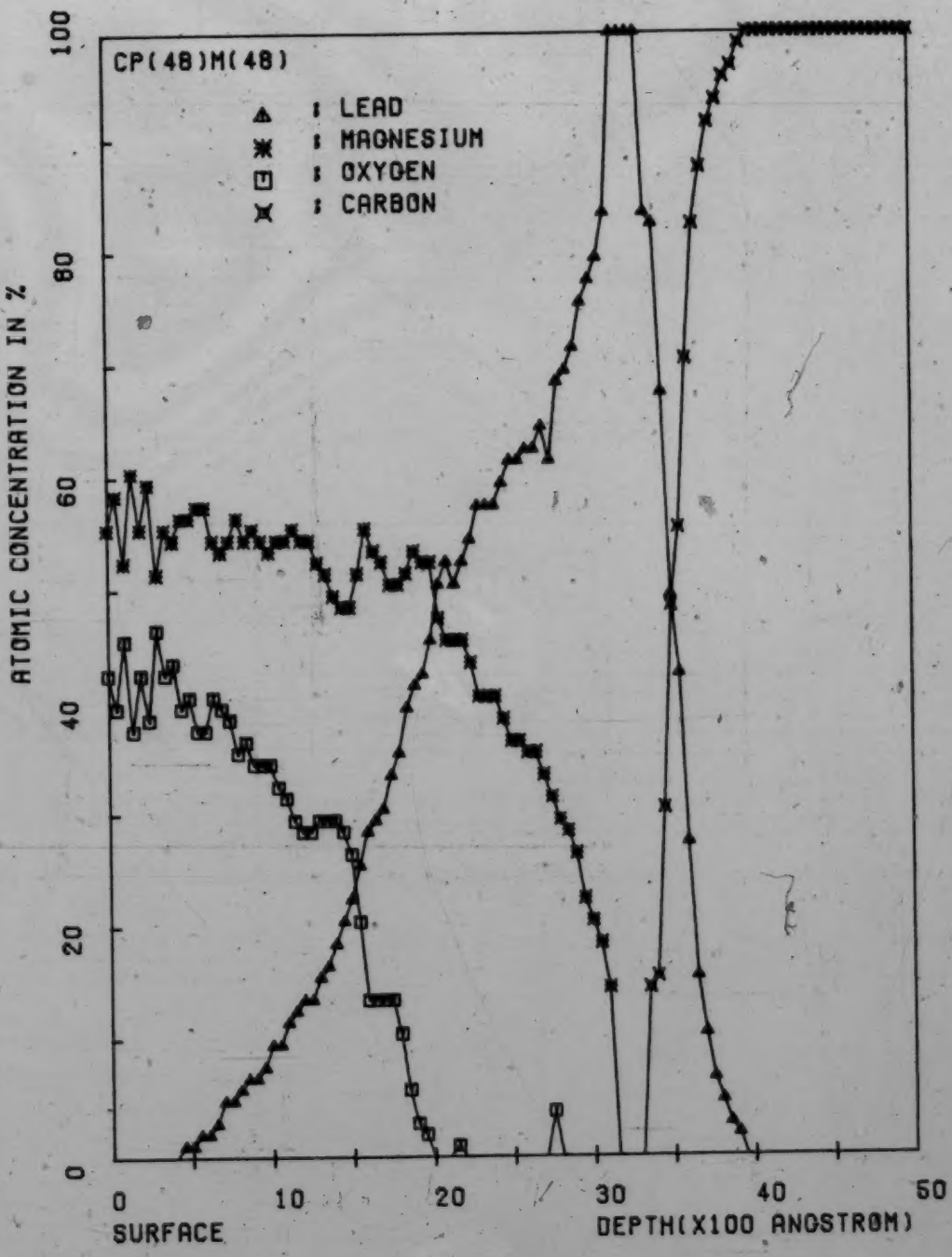

Figure 5-12
Depth profile of CP(48)M(48)

Figure 5-13
SEM surface topography of CM(48) and CP(48)

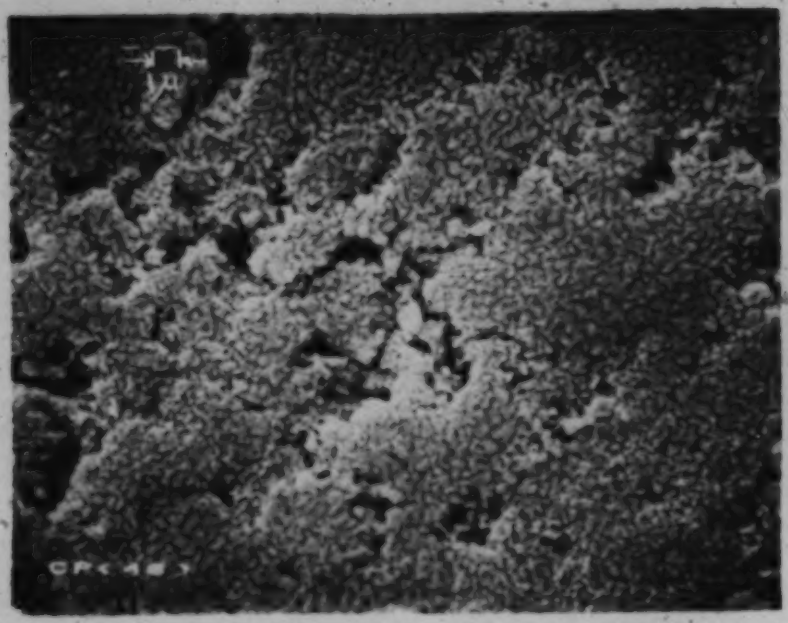

Figure 5-14
SEM surface topography of carbon substrate

CARBON

5.4.4 The surface topography of thermally evaporated and low energy ion beam deposited films.

Figure 5-15 and 5-16 show the surface topography of CM(T) and CM(48), and CM(T)P(T) and CM(48)P(48). A typical distinguishing feature between thermally evaporated films and low energy ion beam deposited films is the grain size. The surface of CM(48)P(48) shows grains of about 2000 Å in size but that of CM(T)P(T) shows no distinguishable grains. Between CM(T) and CM(48) the distinction is seen in the same way, i.e., CM(48) shows very small size of grains but CM(T) shows smoother surface without any observable grains on it. No proof is advanced to explain the differences in the surface structures as a fuction of deposition method but it is postulated that the differences in incident particle energy, growth rate and substrate temperature during deposition by the two methods are the important parameters.

Figure 5-15
SEM surface topography of CM(T) and CM(48)

Figure 5-16
SEM surface topography of CM(T)P(T) nad CM(48)P(48)

1μ
CM<T> P<T>

1μ
CM <48> P<48>

5.4.5 Annealing of CP(T)M(48)

CP(T)M(48) was annealed with four annealing steps(for 30 min. at 100° C, 30 min. at 200° C, 30 min. at 300° C and 250 min. at 320° C). After each annealing step, the target is cooled down to room temperature by injecting Ar gas into the target chamber. A RBS spectrum was taken after the target temperature had been stabilized to room temperature. Figure 5-17 shows the RBS spectra at room temperature, after 30 min. annealing at 300° C and after 250 min. annealing at 320° C. Figures from 5-20 to 5-24 show the derived depth profile for the as deposited and the four annealed ones listed above. A small quantity of lead is observed to move into Mg region after 100° C - 30 min. and 200 - 30 min. annealing step. A greater diffusion of lead is observed after the 300° C - 30 min. annealing step. After the 320° C - 250 min. annealing step, lead appeared on the surface of the film and this two layer region made a compound region of Mg and Pb whose composition ratio ranges from 1 : 1 to 4 : 1 . The diffusion of Mg into Pb region is noticed after 300° C and 320° C annealing steps but the diffused quantity of Mg into Pb is much less than that of Pb into Mg. From depth profile diffusion coefficient of Pb into Mg or Mg

into Pb can be calculated. For example, the number of Pb atoms moved into Mg during 300° C - 30 min. annealing period is derived by comparing the two depth profile taken before and after annealing. It is assumed that the diffusion is carried on only during the annealing period and the small amount of diffusion known to be ocurring even at room temperature(*15) is ignored in this calculation. Figure 5-25 shows the approximated concentration profile of Mg - Pb interface region before and after 300° C - 30 min. annealing. The derived diffusion coefficient of Pb into Mg at 300° C is,

$D = 1.236 \times 10^{-14}$ (cm^2 / sec)

The detailed calculations are given as,

The concentration gradients before and after annealing is,

$dc/dx = 1.806 \times 10^{21}$ atoms/cm^4------ before annealing

$dc/dx = 1.09 \times 10^{21}$ atoms/cm^4------after annealing

The total Pb atoms moved into Mg during annealing period is,

$J \times t = 0.3225 \times 10^{17}$ atoms/cm^2

$J = 1.79 \times 10^{13}$ atoms/cm^2-sec

Diffusion coefficient, D, is given by,

$D = J / (dc/dx)$

taking the average value of dc/dx,

$dc/dx = 1.448 \times 10^{21}$ atoms/cm^4

$$D = 1.236 \times 10^{-14} \text{ cm}^2/\text{sec}$$

The preferrential diffusion of Pb into Mg is observed after 300° C - 30 min. annealing step. No significant diffusion of oxygen is observed after each step of annealing and the low diffusion of Mg into Pb could be the cause of low diffusion of oxygen because the oxygen in the film is in the form of MgO.

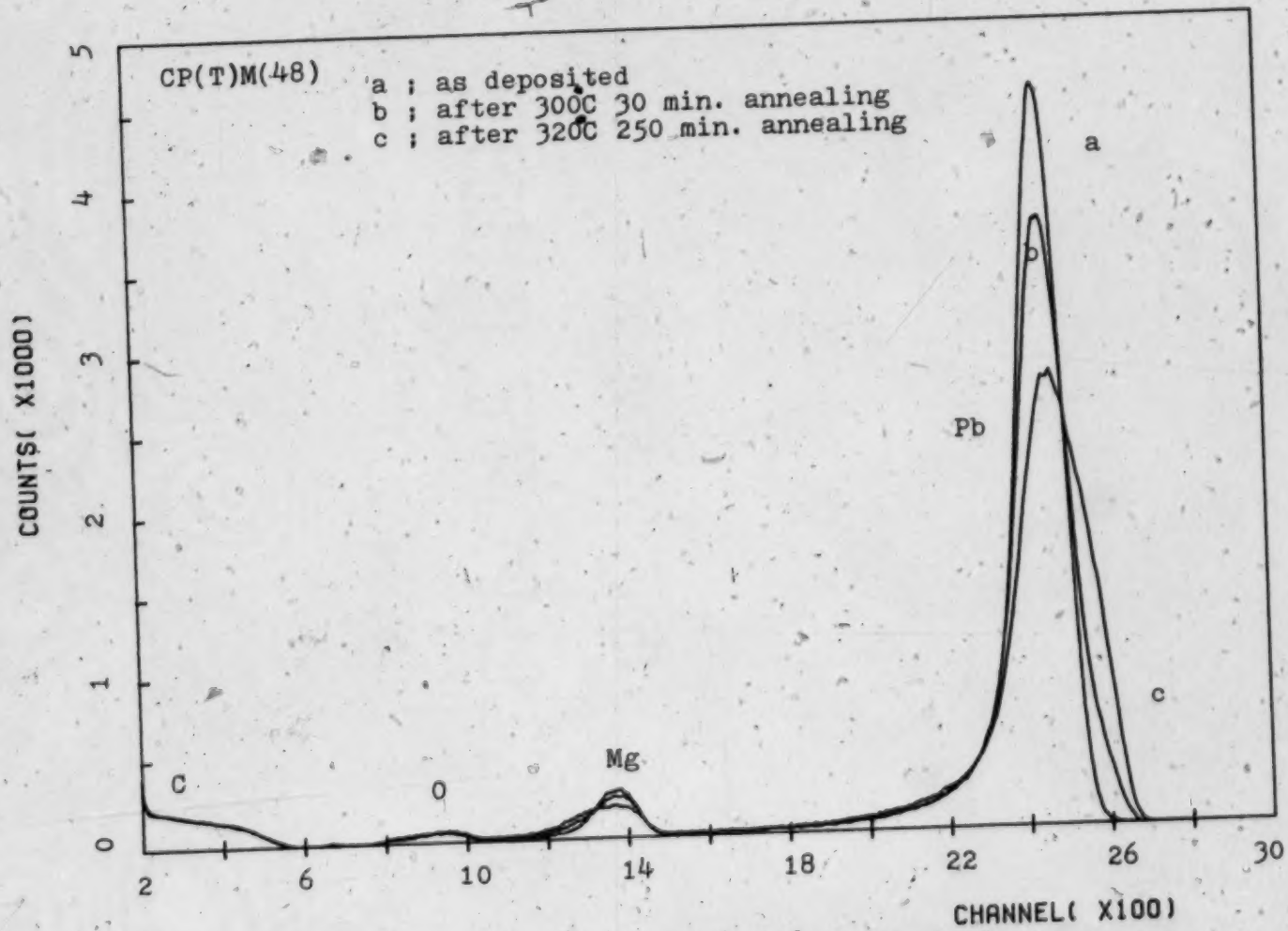

Figure 5-17
RBS spectra of CP(T)M(48) : as deposited, after 300°C-30min. and after 320°C-250min. annealing.

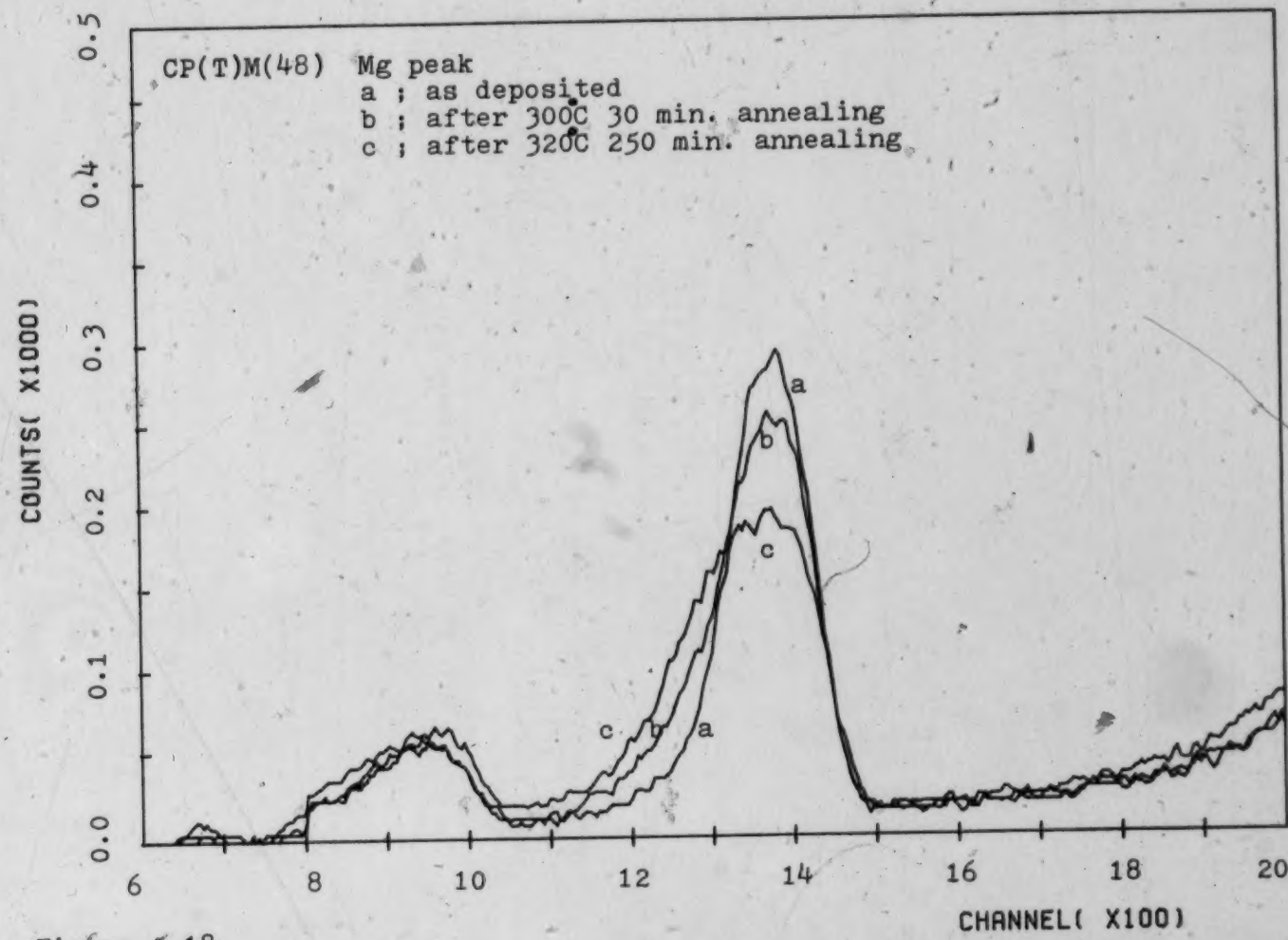

Figure 5-18
Mg and oxygen portion of Figure 5-17 in expanded energy scale

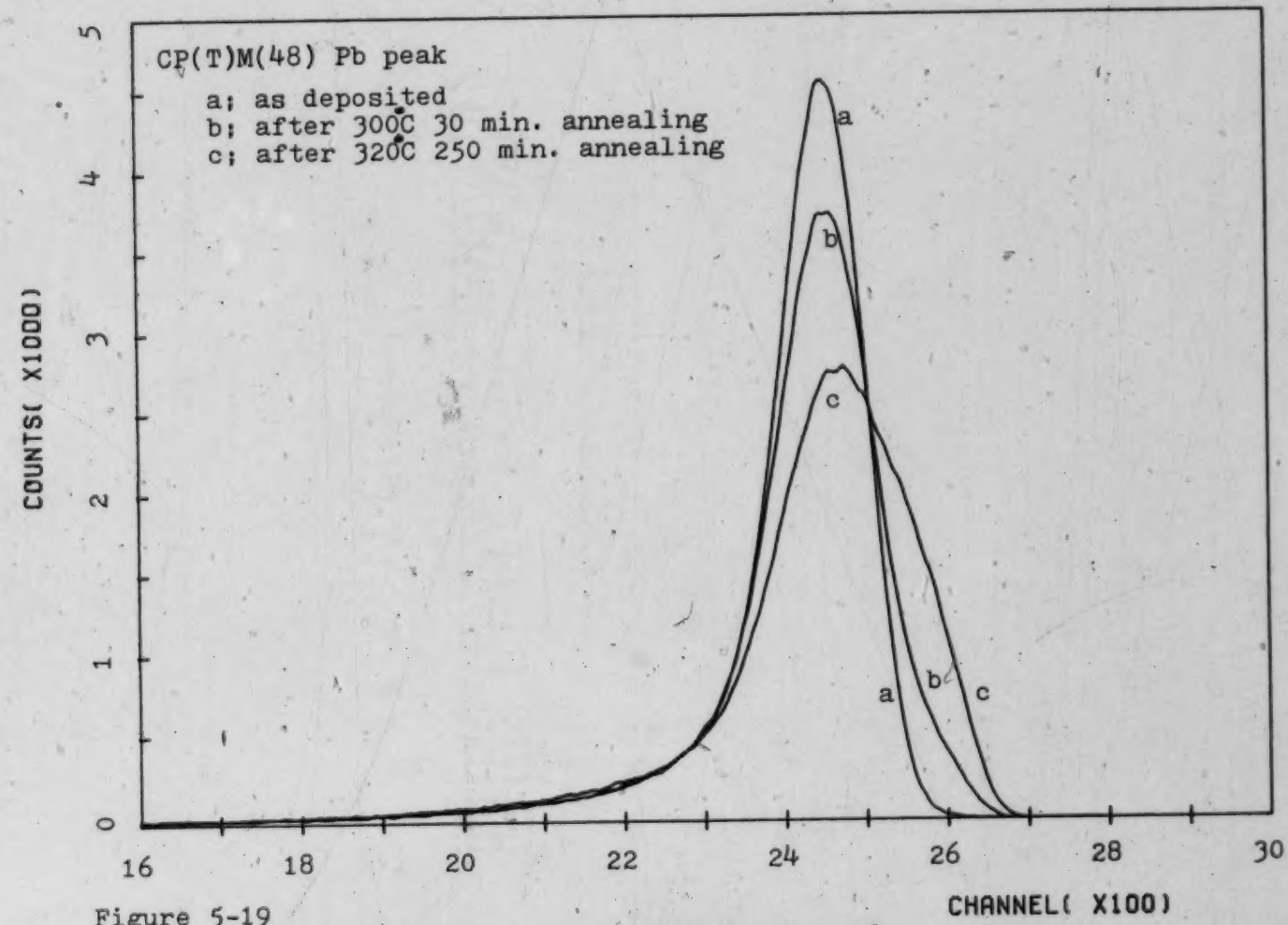

Figure 5-19
Pb portion of Figure 5-17 in expanded energy scale

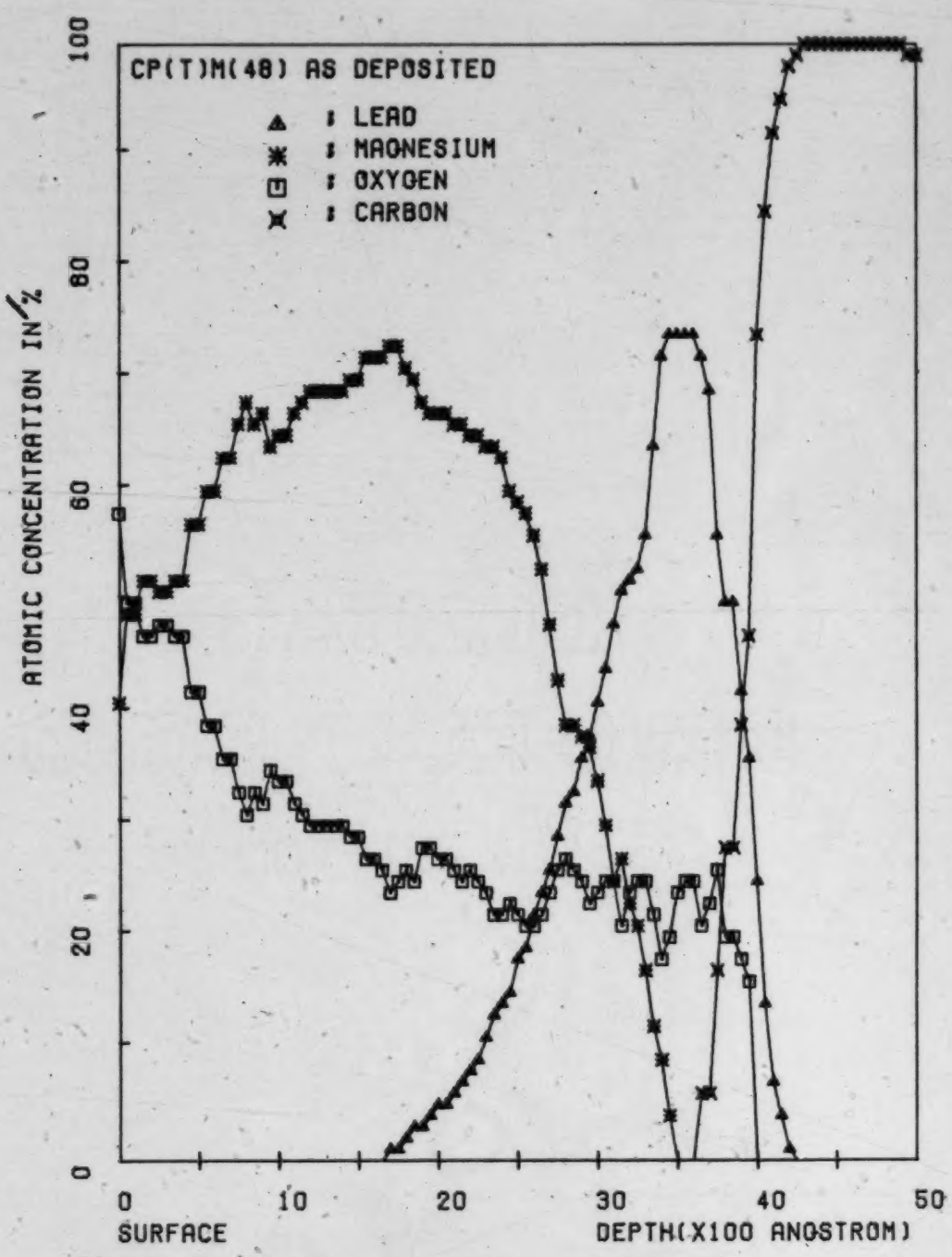

Figure 5-20
Depth profile of CP(T)M(48) : as deposited

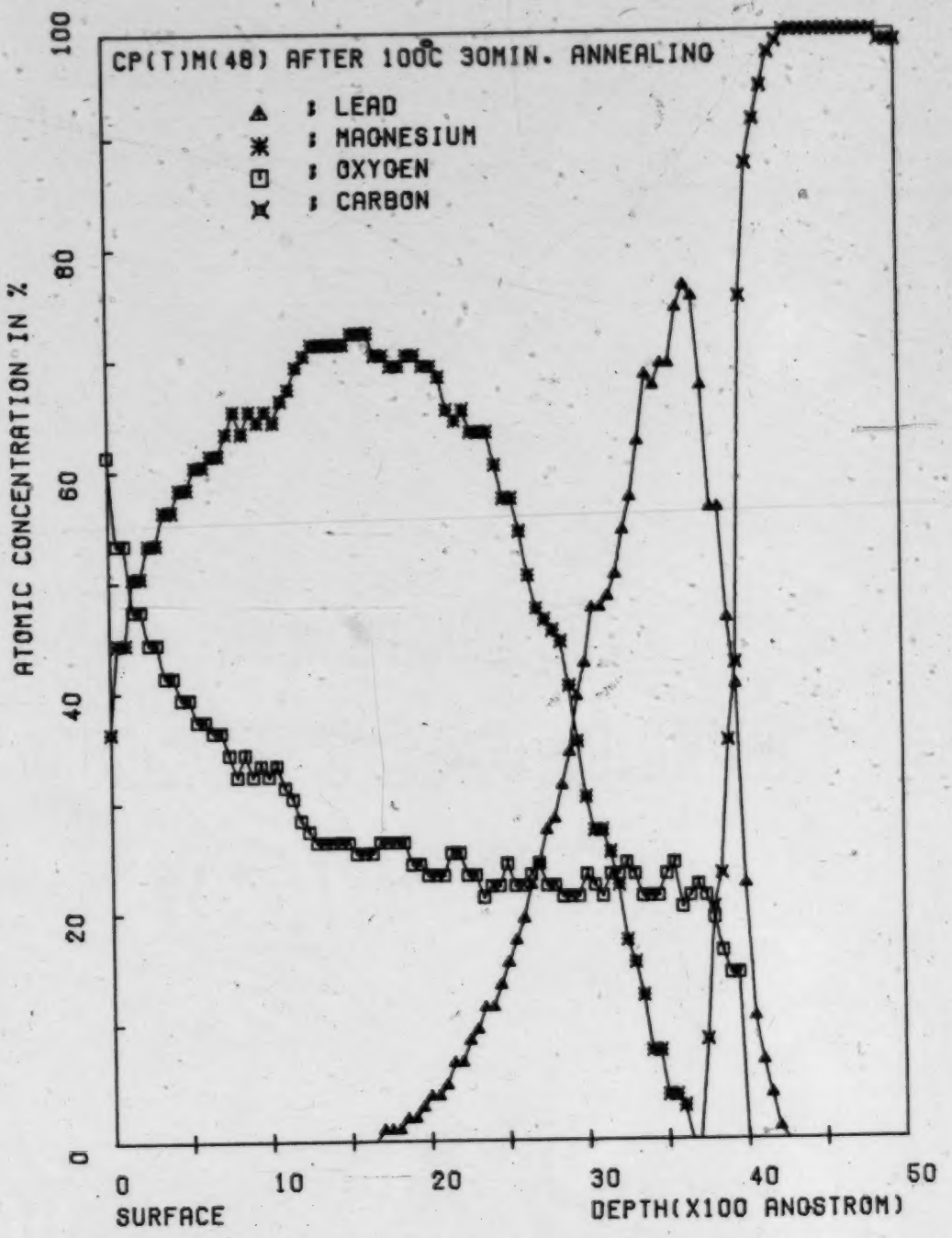

Figure 5-21
Depth profile of CP(T)M(48) : after 30 min. annealing at 100C.

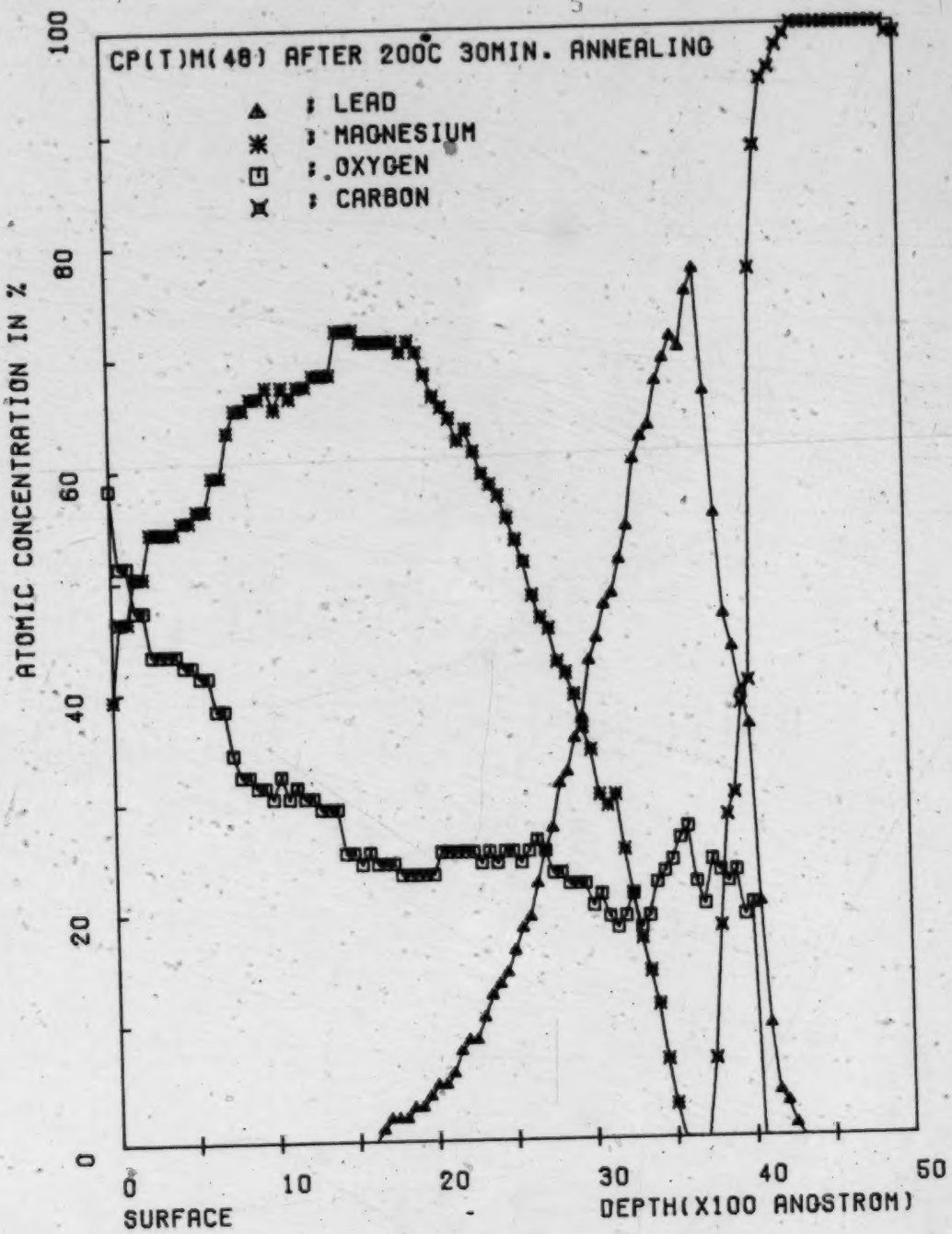

Figure 5-22
Depth profile of CP(T)M(48) : after 30 min. annealing at 200C.

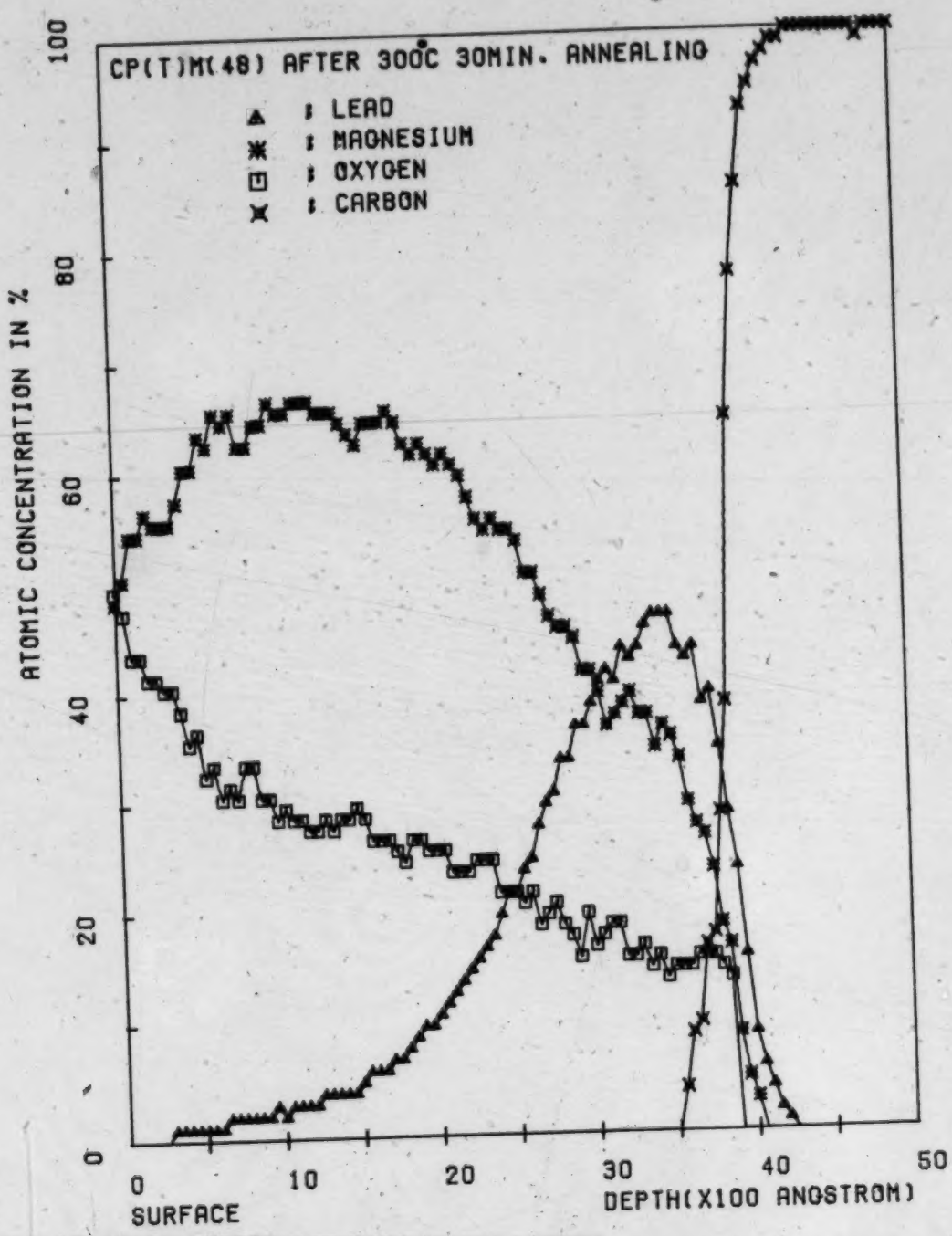

Figure 5-23
Depth profile of CP(T)M(48) : after 30 min. annealing at 300C.

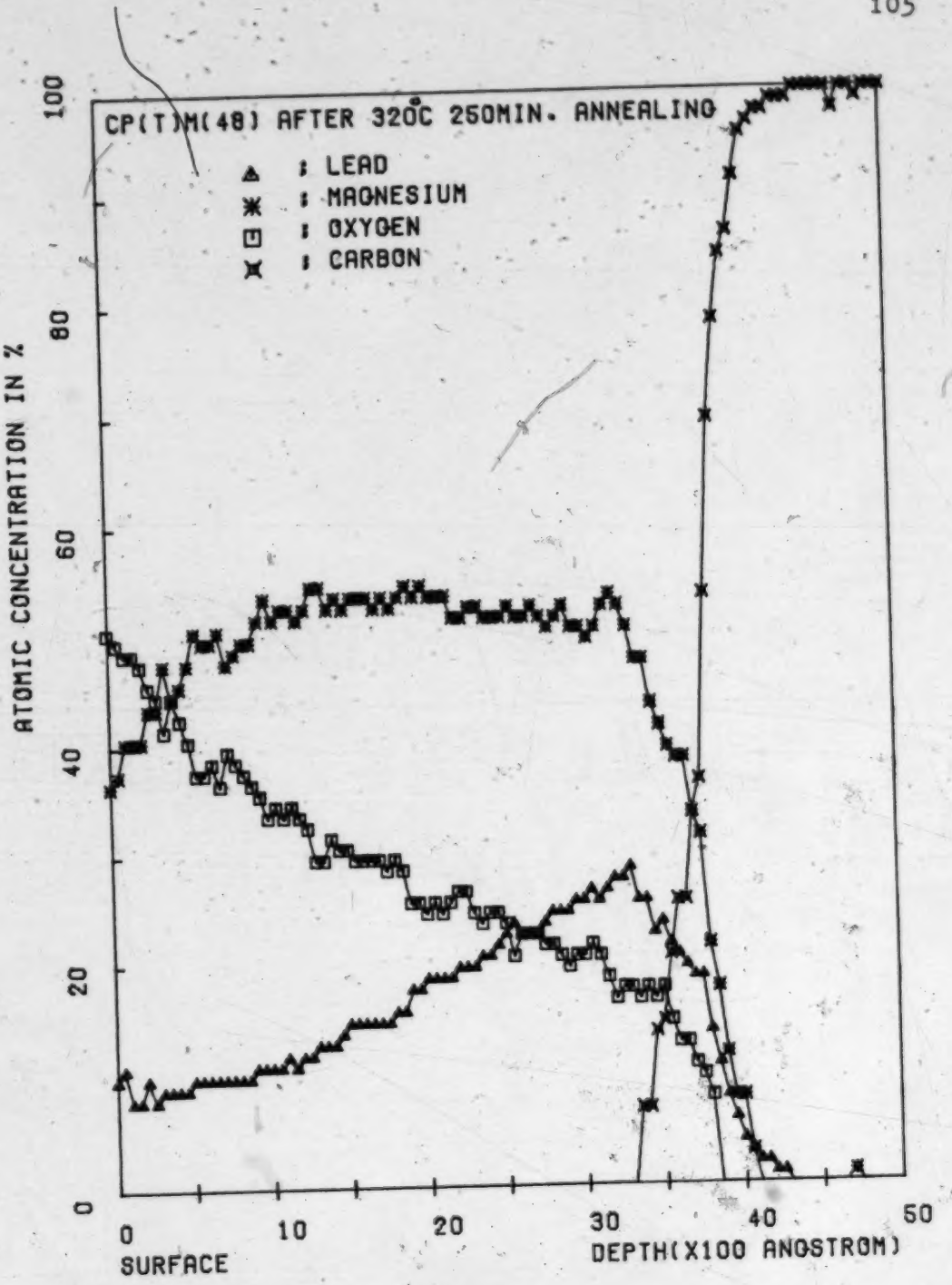

Figure 5-24
Depth profile of CP(T)M(48) : after 250 min. annealing at 320°C.

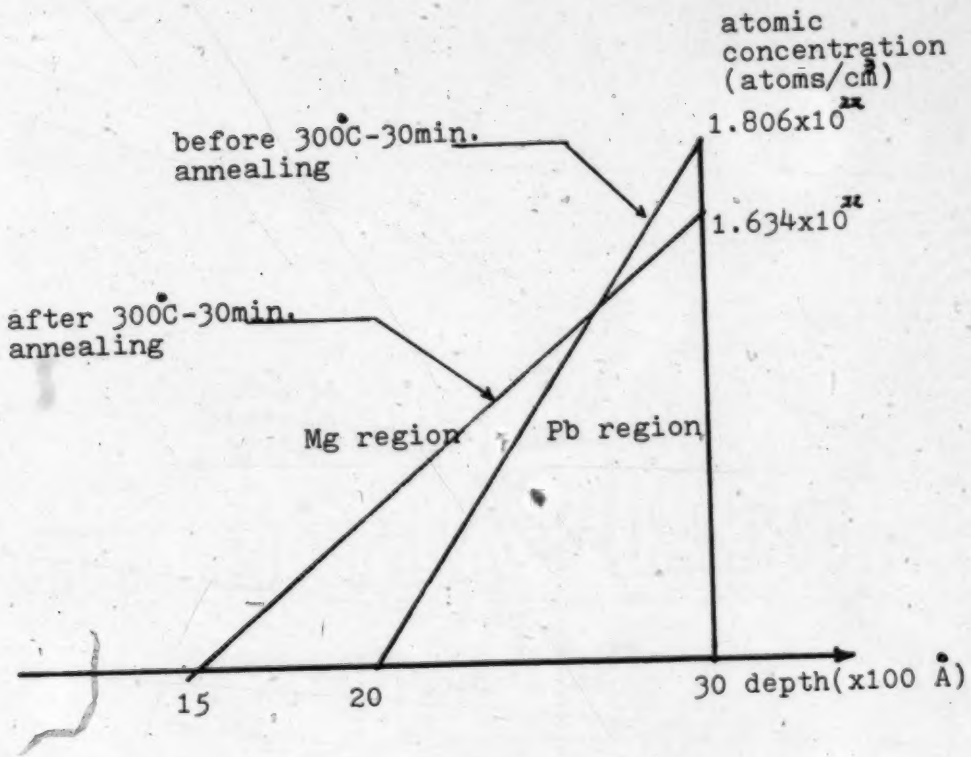

Figure 5-25
Pb atomic concentration slope in Mg region
before and after 300C-30min. annealing.

CHAPTER 6

CONCLUSIONS

This chapter summarizes the present study of low energy ion beam deposited multilayer thin films. First the advantages of low energy ion beam deposition method compared to the conventional methods are summarized and then Rutherford backscattering analysis for compound material is discussed. Finally the investigated characteristics of the multilayer thin films are summarized.

a. The advantages of low energy ion beam deposition method.

   The definite advantage of this method is that it has more controllable deposition parameters than any other conventional methods. The controllable deposition parameters are incident particle energy, film growth rate, particle directionality, pressure during film growth, mass selectivity and particle status. The controllability of deposition parameters gives the controllability of deposited film characteristics.

b. Rutherford backscattering analysis for compound material

   Depth vs. composition ratio profiles are derived from RBS spectra of compound material of Mg,Pb,O and C. A computer program is written for the

derivation of physical profiles from RBS spectra having separated multiple peaks.

c. The investigated film characteristics

1) Both RBS spectra of thermally evaporated film and low energy ion beam deposited film show a high degree of oxygen contamination. This is considered to be a post deposition effect. The involved oxygen does not stay on the surface of the Mg films forming magnesium oxide layer but is dispersed into Mg region.

2) RBS spectra from low energy ion beam deposited Mg film show that isotopes are removed.

3) A preferrential diffusion of Pb into Mg is observed and the difference of grain size between Pb films and Mg films is considered to be the major cause of this result.

4) The derived width of the interface region between Mg and Pb film layer ranges approximately from 1000 Å to 3000 Å and they are not dependent on the film deposition method.

REFERENCES

Chapter 1

1. Chopra,K.L.
   Thin Film Phenomena (McGraw Hill, N.Y. 1969)
2. Glass,A.J., Guenther,A.H.
   Eds. NBC Spec. Pub. 387,372,356.
   Laser Induced Damage in Optical Material(US GPO
   Washington,D.C. 1974,1973,1972)
3. Amano,J. ,Bryce,P. ,Lawson,R.P.W.
   Thin Film Deposition Using Low Energy Ion Beams(1)
   J. Vac. Sci. Technol. 13, 591-595, 1976
4. Amano,J. ,Lawson,R.P.W.
   Thin Film Deposition Using Low Energy Ion
   Beams(2),(3)
   J. Vac. Sci. Technol. 14, 831-835, 836-839, 1977

Chapter 2

1. Carter,G. ,Colligan,J.S.
   Ion Bombardment of Solids (American Elsevier,
   1968)
2. Loc. cit. (1) in chapter 2
3. Hagstrum,H.D.
   Auger Ejection of Electrons from Molybdenum by
   Noble Gas Ions.

Phys. Rev. 104, 672, (1956)

4. Kaminsky,M.
   Atomic and Ionic Impact Phenomena on Metal Surfaces (Academic Press Inc. 1965)
5. Parilis,E.S. Kishinevskii,L.M.
   The Theory of Ion-Electron Emission
   Soviet Phys. Solid State 3, 885, 1960
6. Hagstrum,H.D.
   Theory of Auger Ejection of Electrons from Metal by Ions.
   Phys. Rev. 96, 325, 1954
7. Oliphant,M.L.E., Moon,P.B.
   The Liberation of Electron from Metal Surfaces by Positive Ions.
   Part 2, Theoretical Proc. Roy. Soc. (London) A127, 388, 1930
8. Massey,H.S.
   The Theory of Extraction of Electrons from Metals by Positive Ions and Metastable Atoms
   Proc. Cambridge Philos. Soc. 26, 386, 1930.
9. Shekhter,S.S.
   Neutralization of Positive Ions and Emission of Secondary Electrons.
   J. Exper. Theor. Phys.(U.S.S.R.) 7,750,1937
10. Cobas,A. Lamb,W.E.
    On the Extraction of Electrons from a Metal Surface by Ions and Metastable Atoms

Phys. Rev. 65, 327, 1944

11. Loc. cit. 7 in chapter 2

12. Loc.cit. 6 in chapter 2

13. Hagstrum,H.D.
Theory of Auger Ejection of Electrons from Metals by Ions.
Phys. Rev. 96, 336, 1954

14. Loc. cit. 6 in chapter 2

15. Kittel,C.
Introduction to Solid State Physics(Wiley,1971)

16. A.I.P. Handbook (McGraw Hill, 1963)

17. Loc. cit. 1 in chapter 2

18. Bohr,N.
Mat. Fys. Medd. Dan. Vid. Selsk. 18, No.8,1948

19. Gibson,J.B. Goland,A.N. Milgram,M. Vineyard,G.H.
Phys. Rev. 120, 1229, 1960

20. Gombas,P.
Handbuch der Physik 36, (Springer Verlag Berlin 109, 1956)

21. Cabrera,N.
Discussions Faraday Soc. 28,16,1959

22. Zwanzig, R.W.
J. Chem. Phys. 32, 1173, 1960

23. McCaroll,B. Ehrlich,G.
J. Chem. Phys. 38, 523, 1963

24. Loc. cit. 21,22,23 in chapter 2

25. Loc. cit. 21,22,23 in chapter 2

Chapter 3

1. Amano,J.
Ph.D. Thesis (University of Alberta, 1976)

2. Colutron Velocity Filter Technical Sheet
Colutron Research Coporation, PO Box 1288,Boulder,Colo.,80302, U.S.A.

Chapter 4

1. Chu,W.K. Mayer,J.W. Nicolet,M.A. Buck,T.M. Amsel,G. Eisen,F.
Microanalysis of Surface, Thin Film and Layered Structures by Nuclear Backscattering and Reactions.
(International Symposium on Silicon Material Science and Technology Semiconductor Silicon, 1973)

2. Chu,W.K. Mayer,J.W. Nicolet,M.A. Buck,T.M. Amsel,G. Eisen,F.
Principles and Application of Ion Beam Techniques for the Analysis of Solids and Thin Films.
Thin Solid Films 17, 1, 1973

3. Nicolet,M.A. Mayer,J.W. Mitchell,I.V.
Microanalysis of Materials by Backscattering Spectrometery.
Science 177, 841, 1972

4. Burcham,W.E.
Nuclear Physics (Longman, 1973)

5. Mitchell,I.V. Kamoshida,M. Mayer,J.W.
Channeling Effect Analysis of Thin Films on Silicon:Aluminium Oxide.
J. Appl.Phys. 42, 4378, 1971

6. Loc. cit. 2 in chapter 4

7. Loc. cit. 4 in chapter 4

8. Bragg,W.H. Kleeman,R
Phil. Mag. 10, 5318, 1905

9. Northcliffe,L.C. Shilling,R.F.
Nuclear Data Tables A7, 223, 1970(Academic Press)

10. Feng,J.S.Y. Chu,W.K. Nicolet,M.A.
Bragg's Rule Study in Binary Metal Alloys and Metal Oxides for MeV He Ions.
Thin Solid Films 19, 227, 1973

11. Feng,J.S.Y. Chu,W.K. Nicolet,M.A.
Stopping Cross Section Additivity for 1-2 MeV He in Solid Oxides.
Phys. Rev. B10, 3781, 1974

12. Ziegler,J.F. Chu,W.K. Feng,J.S.Y.
2nd International Conference on Ion Beam Surface Layer Analysis,Karlsruhe,Germany,1975
Ed. Mayer,O. Linker,G. Kappler,F.(Plenum Press, 1976)

13. Ziegler,J.F. Chu,W.K.
J. Appl. Phys. 47, 2239, 1976

14. Loc. cit. 1 in chapter 4

15. Loc. cit. 2 in chapter 4

16. Loc. cit. 2 in chapter 4

17. Ziegler,J.F. Chu,W.K.

Atomic Data and Nuclear Data Table 13, 463,1974

Chapter 5

1. Loc. cit. 4 in chapter 1

2. Amano.J

Ph.D. Thesis(University of Alberta, 1976)

3. ORTEC Semiconductor Radiation Detector Data Sheet

(Model A-022-050-1000)

4. Kaminsky,M.

Atomic and Ionic Impact Phenomena on the Metal

Surface(Academic Press,1965)

5. Ziegler,J.F. Chu,W.K.

Atomic Data and Nuclear Data Tables 13, 463, 1974

6. Lindhard,J. Scharff,M.

Mat. Fys. Medd. Dan. Vid. Selsk, 27, No.15, 1953

...Bonderup,E. Huelplund,P.

Phys. Rev. A4, 562, 1971

7. Loc. cit. 8 in chapter 5

8. Kozina,Z.

A Peak Finding Method for Use in Ge(Li) Spectra

Processing

Nuclear Instr. and Methods. 11, 129, 1963

9. Addiss,R.R.

Oxidation of Mg Crystals Evaporated Films

AGTA Metall., 11, 129, 1963

10. Cohen

Oxidation of Evaporated Magnesium Films

ACTA Metall. 8, 356, 1960

11. Loc. cit. 12 in chapter 5

12. Landsberg,P.T.

J. Chem. Phys. 23, 1079, 1955

13. Shewmon,P.G.

Phys. Metallurgy p383(Amsterdam, North Holland, 1974)

14. Campisano,S.U. Costanzo,E. Rimini,E

Grainboundary Diffusion and Recrystallization in Cu-Pb Thin Fillms.

Philosop. Magz. 35, 1333, 1977

15. Debonte,W.J. Poate,J.M.

Low Temperature Interdiffusion in the Au-Pd and Au-Rh Thin Film Couples.

Thin Solid Films, 25, 441, 1975